THE PENNSYLVANIA STATE UNIVERSITY
SCHREYER HONORS COLLEGE

DEPARTMENT OF BIOMEDICAL ENGINEERING

COMPUTATIONAL MODELING OF THE EFFECTS OF SHEAR STRESS ON VON WILLEBRAND FACTOR PROTEOLYSIS

MICHAEL WILLIAM TRAMONTOZZI
SPRING 2016

A thesis
submitted in partial fulfillment
of the requirements
for baccalaureate degrees
in Bioengineering and Mechanical Engineering
with honors in Bioengineering

Reviewed and approved* by the following:

Keefe B. Manning
Associate Professor of Biomedical Engineering and Surgery
Honors and Thesis Supervisor

Peter J. Butler
Associate Dean for Education in the College of Engineering
Faculty Reader

Margaret J. Slattery
Assistant Professor of Biomedical Engineering and Undergraduate Program Coordinator
Faculty Reader

* Signatures are on file in the Schreyer Honors College.

ABSTRACT

Heart failure continues to be a worldwide epidemic, affecting millions of people each year. Physicians are more frequently treating patients who experience heart failure with ventricular assist devices (VADs) as opposed to heart transplantation, due to the lack of viable donors and the complications that arise from the procedure. Most patients who receive VADs develop some degree of Acquired von Willebrand Disease (AvWD), a bleeding disorder found in patients who have a defective form of the von Willebrand Factor (vWF) protein. The high levels of nonphysiological shear stress imparted on blood components from VADs are believed to cause the proteolysis of vWF and result in AvWD. This investigation seeks to characterize the effects of shear stress on vWF proteolysis using a computational modeling platform. A model was built using COMSOL Multiphysics Software to simulate the stresses experienced by vWF molecules attached to a bead in an optical trap. vWF is modeled as a porous media, and the Brinkman and Navier-Stokes equations are used to analyze the hydrodynamic drag force experienced by the bead. The simulations provide insight into how vWF is sheared by comparing the effective radius of the bead in the optical trap to the height of the porous layer on the bead in the model at a given hydrodynamic force. A correction factor for the actual unfurling of the vWF protein was obtained, suggesting that the experimental optical trap is underestimating the unfurling of vWF molecules. This correction factor can be used to determine the actual extent of vWF unfurling given a set of experimental data, and that information can offer insight into how vWF is unfurled and sheared clinically in patients with medical devices.

TABLE OF CONTENTS

LIST OF FIGURES

LIST OF TABLES

ACKNOWLEDGEMENTS

The scope of my research has been in a constant state of flux since joining this lab in 2013, but I would first and foremost like to thank my thesis supervisor Dr. Keefe Manning for his guidance and support throughout the entire process. Despite many periods of frustration that I felt with this project, Dr. Manning continued to keep me on track and was an integral part of helping me to make progress with my research. This thesis would not have been possible without his vision for the project. In addition, I would like to thank Dr. Peter Butler for his continued interest with this project, and his immense amount of support and expertise in using the COMSOL software. Dr. Butler was always very encouraging and more than welcome to help troubleshoot any issues that I had with my work.

I would also like to thank Shannon Burke and Monica Corsetti, two of the predecessors for this project, for all of their excellent work, introducing me to the research project and helping me to become acquainted with the methods. I would also like to thank Xavier Candela for his continued assistance and help in fine-tuning the model. Each of them were knowledgeable resources for any questions that I may have had.

Lastly, I would like to thank my parents, my grandparents, and the rest of my family for all of their encouragement and support that I have received in my pursuit of a higher education. I could not have made this journey in my life alone, and I can only hope that I make you all proud. Love you guys.

Chapter 1

Introduction

Clinical Significance

Cardiovascular disease (CVD) is one of the leading causes of death in the United States, accounting for 788,000 deaths in 2010, equivalent to 32% of all deaths[1]. The term CVD is an umbrella term used to define an array of medical conditions that affect the cardiovascular system, including heart disease, which is the leading cause of death among all CVDs. In 2010, coronary heart disease alone took the lives of 380,000 people[1]. There are a number of risk factors that affect an individual's likelihood of developing heart disease, including gender, age, weight, ethnicity, and family history. There is a common misconception that heart disease only affects men and older individuals. While these two groups are at a higher risk, heart disease and stroke are still among the leading causes of death for both men and women in the United States of all racial ethnic groups[2]. Of the close to one million people who died of a CVD in 2000, 32% were under the age of 75[2]. If heart disease is diagnosed in its early stages, simple lifestyle changes and medications can help to mitigate side effects. Although some of the risk factors previously mentioned such as age, gender, and family history unfortunately cannot be controlled, the National Heart, Lung and Blood Institute has identified lifestyle changes, such as maintaining a healthy weight, managing stress, and not smoking, to aid in reducing the risk of CVDs[3]. Statin medications to help block cholesterol production may also be prescribed to help reduce the risk of CVDs and heart failure[3].

Although there are methods of reducing one's risks of heart failure, there is no permanent cure for such a condition. With an increasing population suffering from CVD and heart failure each year, a number of different treatment options have begun to emerge. The current preferred method is cadaveric cardiac allograft, more commonly known as heart transplantation; however, this method can give rise to a slew of complications, including rejection, infection, primary graft dysfunction, sepsis, and narrowing of arteries[4]. Age and functionality of the donor heart are among two characteristics that are scrutinized before a procedure is performed.

Another issue with this method is the availability of viable donors. The demand for heart transplantation significantly exceeds the available supply. There have been between 2,000 and 2,500 heart transplants performed a year for the last two decades in the United States alone[5]. As of 2015, the United Network for Organ Sharing (UNOS) reports that there are 4,213 active people in the United States on the waiting list for a heart transplant[6]. This combination of medical complications and lack of donor availability are why medical professionals are searching for other ways to treat heart disease.

Ventricular Assist Devices

An alternative method to treating heart disease involves the implantation of a ventricular assist device. A ventricular assist device, more commonly referred to as a VAD, is a mechanical pump that assists in pumping blood in patients with heart conditions and supporting heart function. VADs can be attached to either the left ventricle (LVAD), the right ventricle (RVAD), or both ventricles (known as a biventricular assist device). Heart disease typically starts in the left ventricle, where oxygenated blood is pumped through the aorta to the rest of the circulatory system. For this reason, LVADs are the most common type of VAD.

Two types of devices exist in the market today: pulsatile-flow VADs and continuous-flow VADs. The two designs differ in the fundamental way in which they circulate blood around the cardiovascular system. A pulsatile-flow mimics a natural heart rhythm and uses positive displacement to transfer blood to the aorta. A cavity inside the pump will expand to receive a volume of blood and contract to displace that blood forward, as shown in Figure 1A[7].

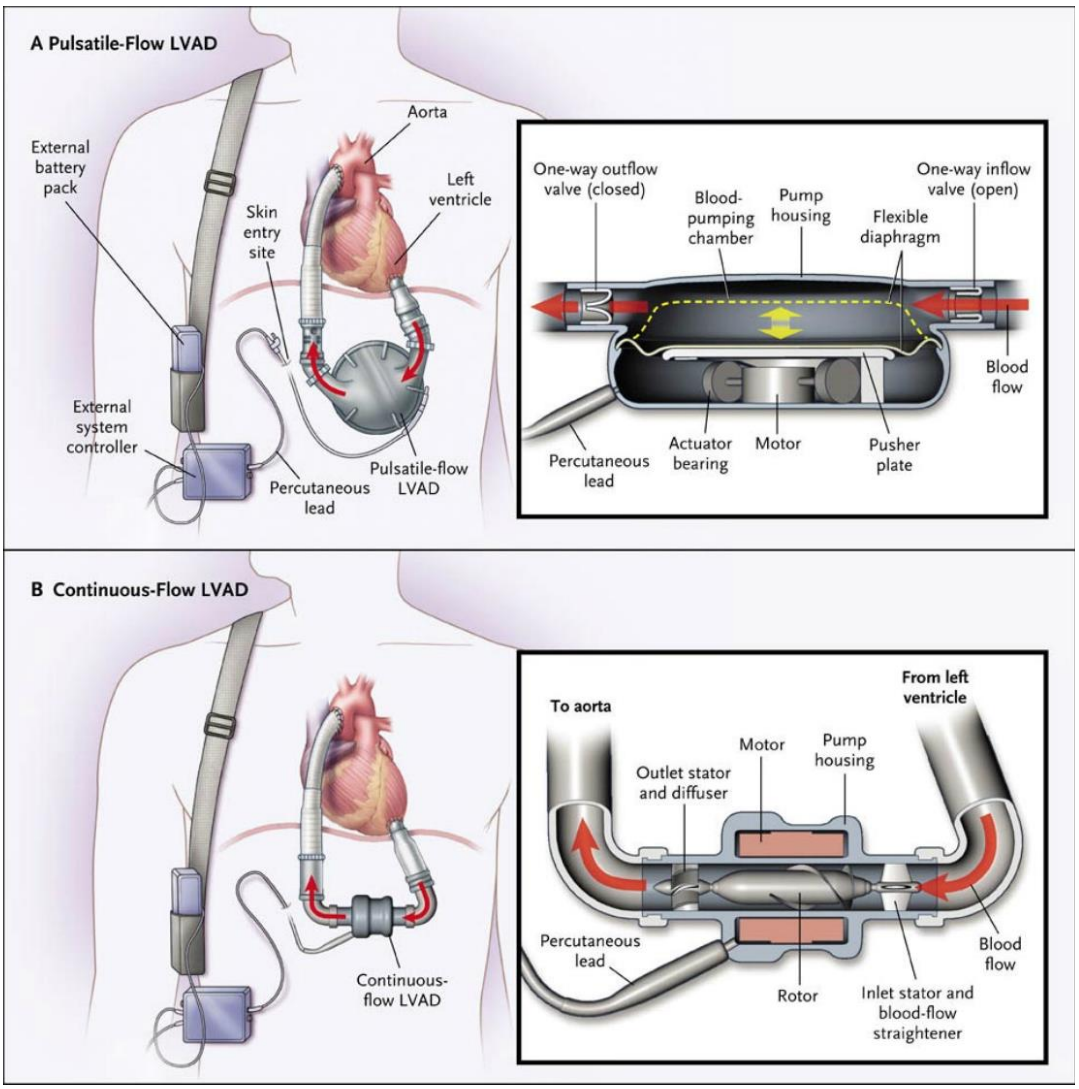

Figure 1. Configuration of a (A) Pulsatile-Flow LVAD and a (B) Continuous-Flow LVAD[7]

Continuous-flow pumps deliver a continuous stream of blood through the cardiovascular system, and rely on centrifugal or axial pumps to displace blood. Axial flow pumps, shown in Figure 1B, have rotors aligned such that blood flow accelerates parallel to the rotor's axis[7]. Older devices used a solid bearing to suspend the rotor, while newer devices contain a singular part that moves due to electromagnetic or hydrodynamic forces. Compared to continuous pumps, pulsatile pumps require a larger housing, a larger intramuscular pump pocket, and are more susceptible to wear and tear due to friction on the bearings over time[8]. Despite this, research has shown that both pumps share the same complications, and that these incidents occur at identical rates[7]. Adverse events can range from immunological rejection problems, such as acute infection, to VAD design problems, such as power interruption/failure. The leading causes of death from patients who have received VADs are hemorrhagic stroke, heart failure, and sepsis[7].

The intent of a ventricular assist device was originally for a short-term bridge to heart transplantation, but VADs have transformed into becoming the staple for managing patients with end-stage heart failure[7]. This use of a ventricular assist device for long-term and/or permanent solution for patients who cannot receive a heart transplantation is referred to as destination therapy. For this reason, there is continued interest in the development of these devices to become more durable and help increase a patient's quality of life.

Acquired von Willebrand Disease

One complication that has been shown to arise in patients who have undergone a VAD implantation is known as Acquired von Willebrand Disease (AvWD)[9]. AvWD, sometimes referred to as AvWS (Acquired von Willebrand Syndrome), is a bleeding disorder found in patients who have a defective form of the von Willebrand Factor (vWF) protein[10]. vWF is a 2813 amino-acid glycoprotein synthesized in endothelial cells and megakaryocytes that is found in blood plasma[11]. This protein is critical to maintaining proper hemostasis and functions in two ways; it is a carrier protein for blood clotting factor VIII, and it also serves as a link between exposed connective tissue at sites of vascular damage and activated platelets[12]. Patients who lack vWF, or have a deficient form of the protein, have defects in platelet deposition and hemostatic plug formation[11]. As a result, these patients can suffer from uncontrollable bleeding episodes.

vWF is comprised of several disulfide-linked 250 kDa multimers and can be >20,000 kDa[12]. The protein is secreted in a globular or coiled form, and becomes activated once the protein unfolds or unfurls. Figure 2 shows how vWF becomes activated in the blood stream.

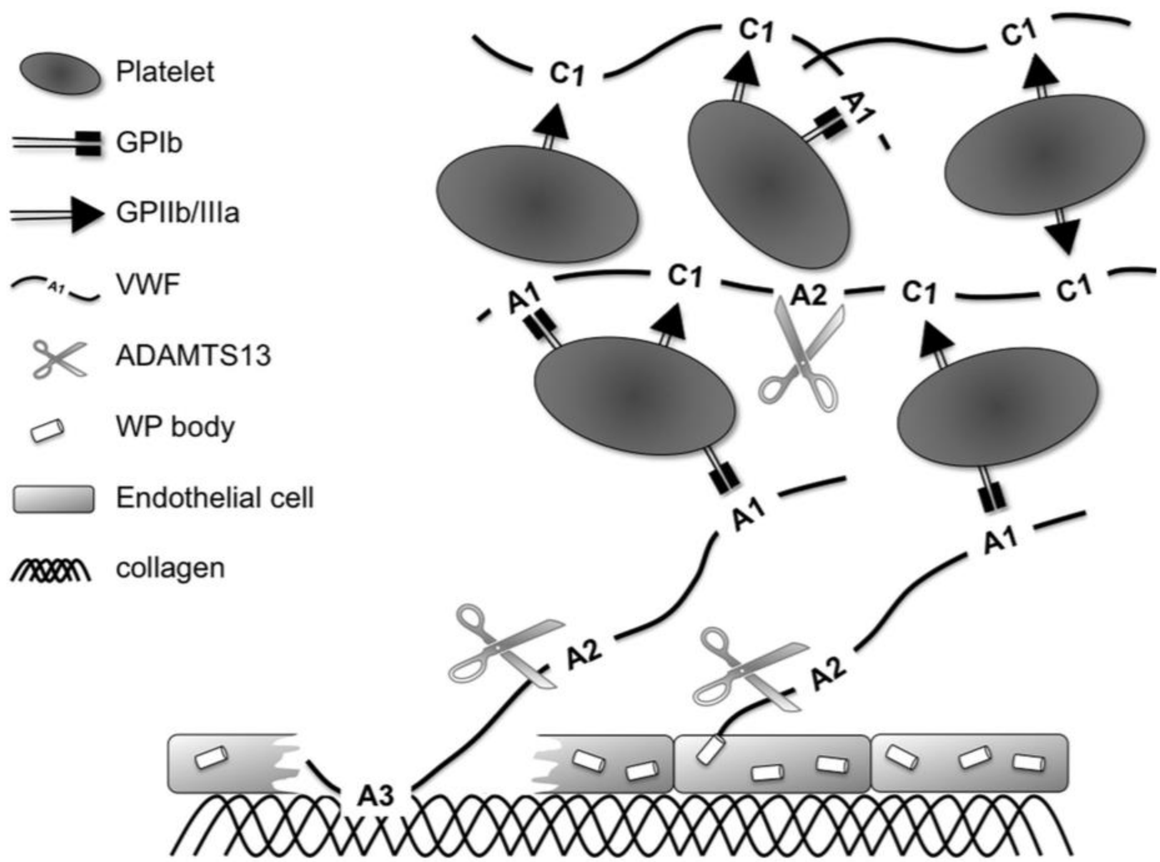

Figure 2. Schematic representation of vWF activation within the blood stream[13]. vWF is immobilized on collagen at its A3 domain after being released from Weibel- Palade (WP) bodies on endothelial cells. Platelets are recruited to the A1 domain by binding to the A1 domain via platelet GPIbα. Once immobilized, vWF can be cleaved by the protease ADAMTS13 at the A2 domain.

Once vWF is excreted by endothelial cells, the protein circulates through the blood stream in its inactive form. At sites of vascular damage, exposed collagen Type I and III binds to vWF at the A3 site shown in Figure 2 and immobilizes the protein[13]. As a result of this, a series of conformational changes exposes the binding site for platelet glycoprotein (GP) GPIbα in the vWF A1 domain[13]. Platelet receptors GpIbα, GpIIb/IIIa, and the GpIb/IX/V complex bind to these sites, forming a platelet plug at sites of blood vessel injury.

The size of vWF multimers is dependent upon the metalloprotease ADAMTS13, which is responsible for the cleavage of vWF at a single peptide bond in the A2 domain, shown in Figure

2. The A2 domain consists of 193 amino acids[14] and is believed to be susceptible to ADAMTS13 due to its high-affinity binding site to the protein[15]. The precise mechanisms in which ADAMTS13 proteolyzes the vWF complex are still unknown; however, proteolysis can only occur once the vWF protein has uncoiled from its inactive globular state. Once vWF has uncoiled, ADAMTS13 truncated mutants recognize and bind to the C-terminal region of the A2 domain[15]. These mutants cleave vWF at the Tyr-842/Met-843 peptide bond in the A2 domain, shown in Figure 3. Initial cleavage produces the 140 kD monomer, while subsequent cleavage produces a 176 kD dimer[16]. Larger multimers of vWF have been observed, such as 200 kDa and 350 kDa multimers; however, these larger multimers are dimers of the 140 kDa and 176 kDa fragments, respectively[16].

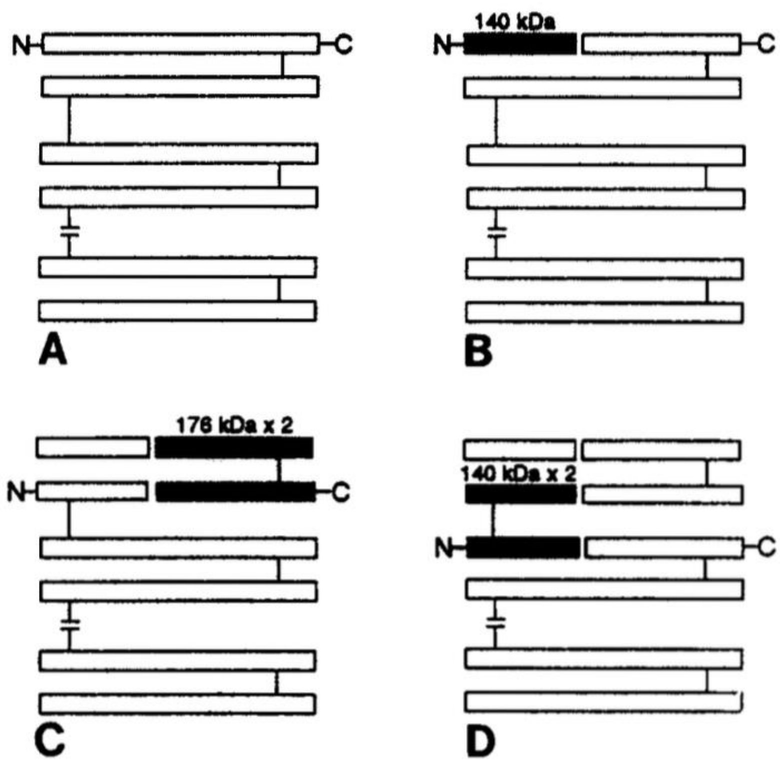

Figure 3. A schematic model of a vWF polymer and its proteolysis at the Tyr-842/Met-843 peptide bond[16]. (A) shows the vWF after it has been secreted by endothelial cells. Two vWF polypeptides are linked by disulfide bonds. (B) shows a cleavage of vWF into the 140 kDa monomer. (C and D) show continued cleavage of vWF generating a 140 kDa and 176 kDa fragment.

Patients who receive a VAD have been observed to experience inexplicable bleeding events post-operation[10]. This non-surgical bleeding experienced by VAD patients is hypothesized to be related to AvWD[9,10,17]. This hypothesis is supported by the notion that one of the causes of AvWD has been linked to high levels of shear stress[15,16]. High levels of shear stress occur in VADs constantly due to the rotating nature of the pump, with shear rates well over 10,000 s^{-1} in different regions[18]. AvWD is characterized by the loss of large multimers of vWF, and patients who receive VADs have been observed to have decreased levels of high molecular weight (HMW) multimers[17]. These losses, in effect, force the protein to become ineffective in the process shown in Figure 2.

Interesting to note is that patients experience a loss of HWM multimers of vWF after the VAD has been implanted, but do not experience that loss after the VAD has been taken out[17]. The vWF protein returns back to its original form immediately after the VAD is removed. The correlation between the high levels of shear stress present in VADs and the loss of HMW multimers in patients who have received VADs suggests that the high shear stress experienced plays a role in the proteolysis of vWF.

Effect of Shear on vWF Proteolysis

There has been a great deal of research done to study the effects of shear stress on the unfolding of vWF, and the subsequent proteolysis. Hematologist Dr. Han-Mou Tsai showed that vWF unfolding is a significant factor in the mechanism of vWF proteolysis. In his experiment, normal plasma was incubated *in vitro* with a purified plasma protease, with a molecular mass of approximately 200 kDa, in the presence of Tris-Buffered Saline (TBS)[11]. It was observed that in the presence of TBS, vWF was not proteolyzed. Another sample of plasma was incubated in the same manner, but in the presence of TBS and Guanidine Hydrochloride (HCl). Guanidine HCl is a solution known to cause unfolding of vWF. vWF cleavage was observed to increase with increasing concentrations of Guanidine HCl, recommending that vWF unfurling is a factor in proteolysis[11].

Tsai *et. al* also used *in vitro* methods to subject blood plasma to known shear rates that are observed *in vivo*. His work showed that larger multimers of vWF appeared to decrease, and smaller multimers of vWF appeared to increase, as the shear rate increased[16]. Specifically, a 200 kDa and 350 kDa band of vWF was observed to increase in concentration upon shear exposure. Elution and immunoblotting studies showed that the 200 kDa band was a dimer of the 140 kDa monomer of vWF, and the 350 kDa band was a dimer of the 176 kDa monomer of vWF[16]. The analysis of the vWF fragments was qualitative in nature. Five different shear rates were tested by Tsai *et. al* and they included 394, 819, 1774, 3327, and 5603 s^{-1}. The greatest band intensity of the 200 kDa and 350 kDa vWF dimers were at higher shear rates, more specifically 3327 s^{-1} and 5603 s^{-1}, suggesting that higher shear rates lead to higher rates of proteolysis.

Atomic Force Microscopy (AFM) has shown that vWF unfurls over time with increased shear stress[19]. An image was taken of a vWF molecule under no load, from an AFM probe force, and using a rotating disk to induce a shear. Figure 4 shows how the vWF molecule unfurls with induced shear stress.

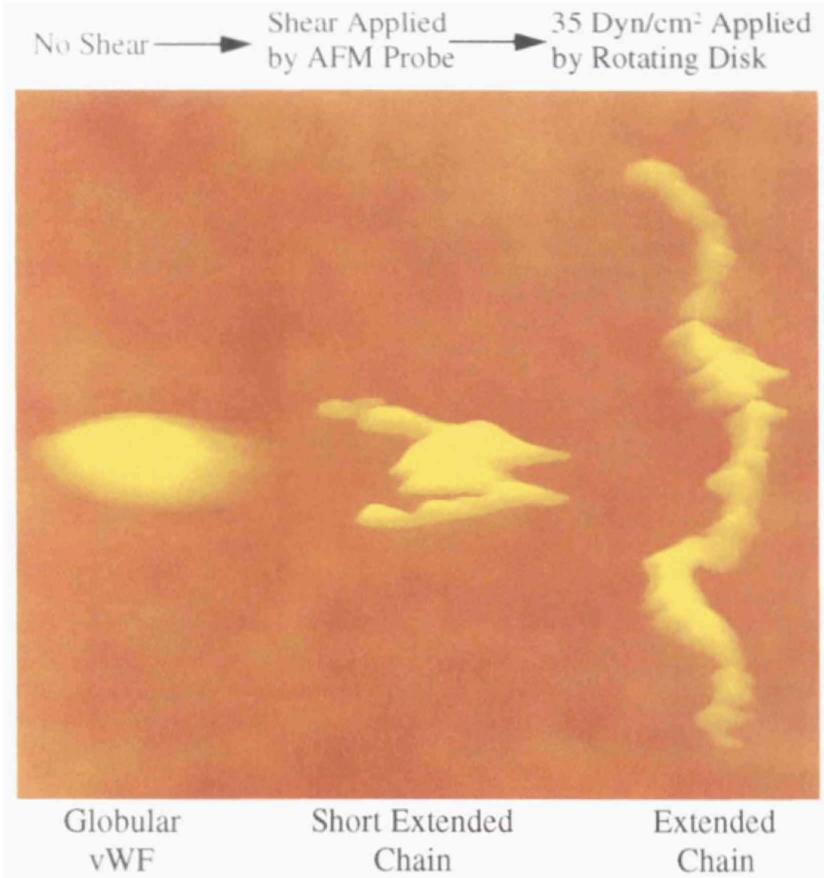

Figure 4. Schematic model using AFM imaging showing how a vWF molecule unfolds and changes orientation when subjected to shear[19]. The left side of the image shows the vWF protein in its normal state. There is no shear applied and the molecule is folded over itself

The shear forces were applied to vWF using the AFM probe tip and a rotating disk system[19]. The manner in which these forces were applied is intended to reflect how free vWF in the bloodstream is stressed during a VAD patient's normal blood flow. The rapid change in velocity of shear flow due to the VAD pump elongates vWF molecules. These changes are heightened in patients with VADs due to the force from the mechanical pump. These stresses can uncoil the vWF molecule and expose a single A2 binding domain for proteolysis at known tensile forces[14,20].

Already active vWF molecules at a site of vascular damage are also subjected to shear stresses due to blood flow. The active vWF molecule is anchored to the vascular site of injury at the A1 domain while the rest of the protein is freely subjected to the blood flow past it. This situation can also induce unfolding of the A2 domains, but the amount of force to do so is currently unknown[14]. There have been several experiments carried out in order to learn more about this phenomenon.

One method to obtain more information about the shearing of a stabilized vWF molecule is with the use of an optical trap. Zhang *et. al.*[20] uses an optical trap with two beads that are each bound to a double-stranded DNA handle. A single N-glycosylated A2 domain was coupled to the DNA handles and suspended between two beads, which were held in place by an optical trap and a micropipette, as shown in Figure 5[20].

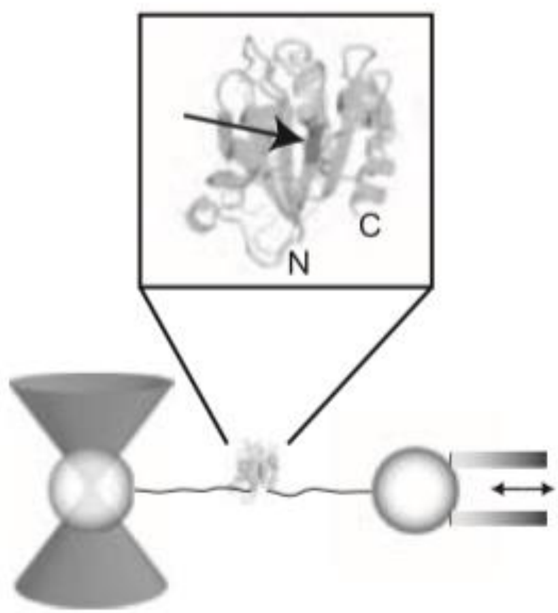

Figure 5: Experimental setup for Zhang *et. al.*[20] The A2 domain of vWF is connected to beads which are held in place by an optical trap (left) and a micropipette (right) via DNA strands.

The micropipette was moved away from the optical trap using a piezoelectric stage in a cyclical fashion, subjecting the bead to various forces seen *in vivo*, in order to determine which stresses cause the A2 domain to unfold[20]. A2 domain unfolding was characterized by measuring changes in molecular length of the vWF molecule. Ying *et. al.*[14] used the same technique in their experiment to show that vWF initially unfolds at an unloading force of 21 pN. Building upon this information, Pennsylvania State University undergraduate students Monica Corsetti[21] and Xavier Candela[22] performed experiments to simulate *in vivo* conditions using an optical trap to fixate a single polystyrene bead containing vWF. The vWF on the bead initially existed in its globular form. The oscillations of a piezoelectric stage were used to induce fluid flow over the bead. The flow over the bead induces a stress on the vWF molecules in order to unfold the protein. Changes in the bead motion and the effective radius of the bead were measured to determine the degree of unfolding of the vWF molecules. A depiction of how the structure of vWF is changing as shear is applied is shown in Figure 6.

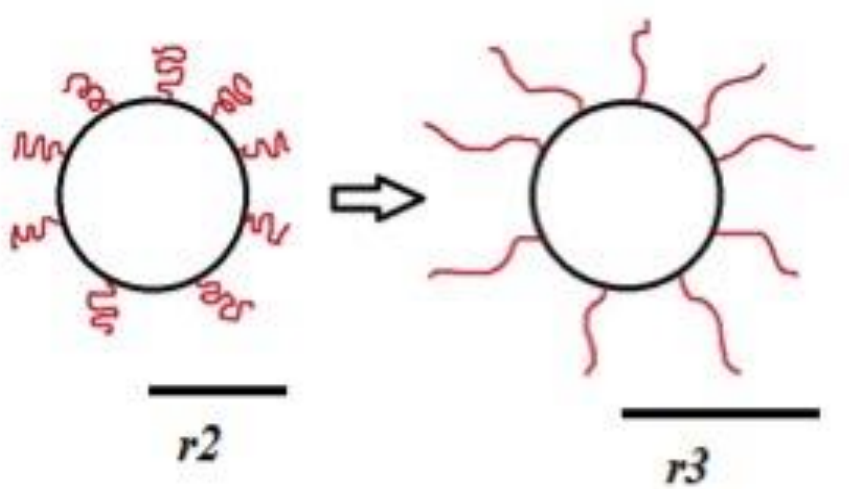

Figure 6. A depiction of vWF molecules adhered to the surface of a polystyrene bead[21]. The bead on the left contains vWF in its globular form before shear is applied. Once shear is applied to the bead, vWF will begin to unfold while staying attached to the bead. The bead on the right demonstrates this effect. R2 and R3 show the effective radius of the bead, and that this radius is larger as the protein unfolds.

There is evidence to suggest that induced-shear on von Willebrand Factor protein results in the unraveling from the proteins globular shape, and that this unraveling makes the protein more susceptible to proteolysis by ADAMTS13.

Finite-Element Analysis in Biomedical Applications

In recent years, finite-element analysis (FEA) has become a more prevalent way to obtain information about a system. FEA uses numerical methods to find approximate solutions to problems for a number of different physics, including solid mechanics, fluid mechanics, and heat transfer. FEA is becoming more commonplace in research and industry as software is becoming more advanced and producing quick and reliable results without having to go through the arduous and costly process of experimental testing. FEA has been used in a variety of different industries, including those for biomedical applications.

One model seeks to model the *in vivo* stresses on the glycocalyx. The plasma protein-rich surface layer of endothelial cells, known as the glycocalyx, is subjected to hemodynamic forces depending on the location in the vasculature, the heart rate, and the metabolic demands of tissues. These forces from the surrounding fluid lead to localized intracellular signaling because the endothelial cells are sensitive to shear[23]. The shearing forces acting on endothelial cells affect the overall morphology, structure and function of these cells *in vivo*[24]. The glycocalyx is a complex surface that responds to changes in shear in a number of ways. Experimental observations suggest that cell responses to stress can be modeled using linear elasticity, tensegrity, poroelasticity, viscoelasticity and power-law rheology[23].

The model looks at the glycocalyx layer as a poroelastic surface that surrounds the endothelial cell surface. A fluid was introduced to flow over the top of the poroelastic layer. The resulting drag force from the fluid was calculated using a model based on the Brinkman equation, which involved adding the drag force due to shear stress at the top of the Brinkman layer to the force per unit volume due to drag on the poroelastic surface, modeled as idealized vertical strands[23]. This model relied on determining a parameter known as the Darcy permeability in order to calculate the force and displacement. Other models have used this same permeability constant to model bending moments on microvilli[24]. In each of these models, a physiological system of many cells was simplified into a uniform matrix, and a set of governing equations was used to solve for force and displacement.

Applying this same concept to the work of Corsetti[21] and Candela[22], who tested vWF in an optical trap, a model can be created to computationally calculate the stresses and strains on vWF molecules due to the movement of a piezoelectric stage. Several vWF molecules are adhered to the surface of polystyrene beads. One end of vWF is fixed to the bead and the rest of the glycoprotein is subjected to shear, due to the velocity gradient that exists around the bead. This more closely resembles the *in vivo* situation in which vWF is immobilized on one end when connected to collagen and the other end of the protein is subjected to blood flow. The inlet velocity of the optical trap can be altered to obtain different stresses and study the rate of vWF unfurling.

The experimental optical trap data assumes that the densely packed vWF on the outside of the bead act as a solid shell when determining the effective radius. A simplified model representing these vWF molecules as a uniform porous matrix in which fluid can flow through the matrix more accurately models what is happening experimentally since fluid flow is occurring between vWF molecules. The governing equations of the matrix and the fluid flowing around the matrix can be used to characterize the shear forces and displacements that exist on this surface due to an increase in shear. The numerical model is believed to be more accurate at depicting the unfurling of vWF in an optical trap than the experimental model. Comparing values from the numerical simulations to values found experimentally, a correction factor for the amount of vWF unfurling can be obtained and used for future experimental studies.

This numerical model seeks to characterize the relationship between shear and vWF proteolysis in an optical trap by determining the actual unfurling of a sheared vWF molecule. This study seeks to build upon the work demonstrated by Zhang *et. al.*[20], Ying *et. al.*[14] and Pennsylvania State University undergraduate students Monica Corsetti[21] and Xavier Candela[22].

Chapter 2

Materials and Methods

Computational Modeling

This thesis looks to computationally model the effects of shear stress on von Willebrand Factor proteolysis in an optical trap. Computationally, COMSOL Multiphysics 5.2 software (COMSOL Inc., Burlington, MA) will be used to model the stresses imposed on a porous layer coating on the surface of a polystyrene bead that is subjected to fluid flow. This was done by modeling the vWF molecules as a porous media around the bead. The model is assuming that the collection of vWF molecules around the bead are acting as a solid material with empty internal pore structures. A 2D Couette two-fluid model was created both analytically and numerically in order to validate the 3D optical trap model. The purpose of this model was to gain an understanding for how COMSOL is defining specific parameters in the software.

Analytical Model of a 2D Two-Fluid Couette Flow

The original model of the optical trap was validated using a 2D Couette flow consisting of two fluids, which is shown in Figure 7. A no-slip wall is considered on the bottom boundary. Fluid 1 has a viscosity value which is greater than that of fluid 2, which is modeled as water. A moving wall, denoted by the blue arrow, is driving the flow in the system. This model is not exactly modeling the optical trap situation, in which flow is stressing and uncoiling the vWF molecules, but rather it is more similar to flow past a flat plate containing a highly viscous gel.

.

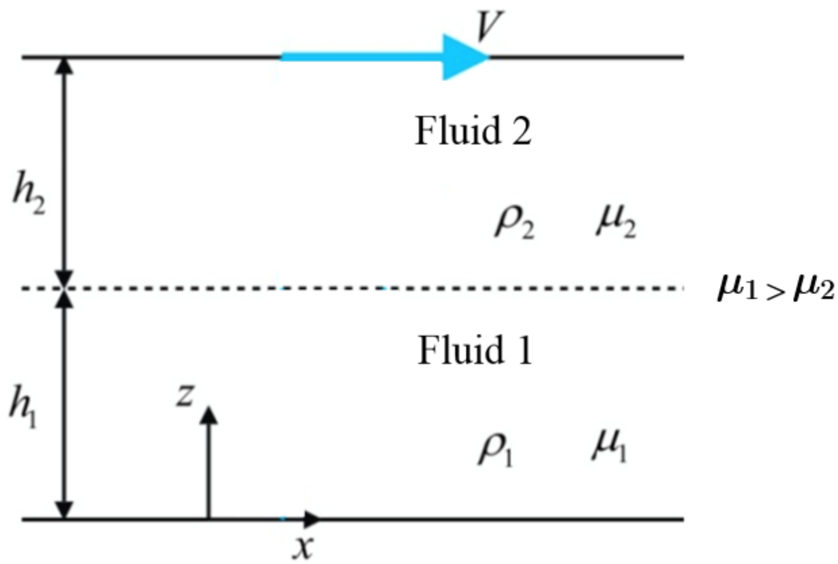

Figure 7. Diagram of the 2D two-fluid Couette flow case[25]

The velocity profiles for each fluid were derived by integrating the x-momentum equation for parallel, fully developed flow shown in Equation 1, given the boundary conditions outlined in Equations 2-5.

$$\frac{\partial^2 u}{\partial^2 z} = 0 \qquad \text{Equation 1}$$

$$At\ z = 0,\ u_1 = 0 \qquad \text{Equation 2}$$

$$At\ z = h_1 + h_2,\ \ u_2 = V \qquad \text{Equation 3}$$

$$At\ z = h_1,\ \ u_1 = u_2 \qquad \text{Equation 4}$$

$$At\ z = h_1, \mu_1 \frac{du_1}{d_z} = \mu_2 \frac{du_2}{d_z} \qquad \text{Equation 5}$$

Equation 2 assumes the no slip condition at the wall. Equation 3 states that the velocity at the free surface is equal to the velocity of the moving plate. Equation 4 states that the velocity of both fluids at the interface must be equal. Equation 5 states that the shear stress of both fluids at the interface must be equal. After integrating Equation 1 and applying the boundary conditions in Equations 2-5, the solutions for the velocity in each layer were obtained and are outlined in Equations 6 and 7. The shear stress and shear rate in each of the two fluids, which were used during the analysis, are defined by Equations 8 and 9, respectively.

$$u_1 = \left[\frac{\mu_2 V}{\mu_2 h_1 + \mu_1 h_2}\right] z \qquad \textbf{Equation 6}$$

$$u_2 = \frac{V}{\mu_2 h_1 + \mu_1 h_2}\left[\mu_1 (z - h_1) + \mu_2 h_1\right] \qquad \textbf{Equation 7}$$

$$\tau = \mu \frac{d_u}{d_y} = \mu\gamma \qquad \textbf{Equation 8}$$

$$\gamma = \frac{u_2 - u_1}{h_2 - h_1} \qquad \textbf{Equation 9}$$

The parameters for this model were defined so as to be similar to that of the optical trap experiments performed by Candela[22]. When solving these equations, the height of fluid 1, h_1, was selected to be 900 nm, as this is a length of vWF that has been previously observed[26]. The height of fluid 2, h_2, was specifically determined to achieve a shear rate of 1250 s^{-1} in fluid 2. The shear rate was chosen based upon the parameters Candela was using in his optical trap experiment[22]. Equation 7 and Equation 9 were used to determine h_2. The two equations contained two unknowns, the height of fluid 2 (h_2) and the velocity at the interface (u_1 when $z = h_1$). Since neither of this variables were known, and the two variables were dependent of each other, values for these two parameters were obtained by estimating values and performing multiple iterations in order to determine the true values. The true value for h_2 was determined to be ~0.14 µm.

The velocity V was chosen to be 0.62831 mm/s, which corresponds to the 1250 s^{-1} shear rate[22]. The dynamic viscosity of fluid 1 was obtained by assuming the viscosity of the viscous layer was similar to that of a DNA solution. There have been research studies to determine the viscosities of solutions with different DNA concentrations. The viscosity was assumed to be 0.0025 Pa·sec[27]. The viscosity of fluid 2 was 0.001 Pa·s, which is the viscosity of water.

Computation Model of a 2D Two-Fluid Couette Flow

In addition to solving these equations analytically, the 2D Couette flow was simulated numerically in COMSOL with a laminar flow physics. The governing equations for the model were the Continuity and Navier-Stokes equations, defined by Equations 10 and 11, respectively,

$$\nabla \cdot \mathbf{v} = 0 \qquad \textbf{Equation 10}$$

$$\rho \frac{Dv}{Dt} = -\nabla p + F + \mu \nabla^2 v \qquad \textbf{Equation 11}$$

where μ is the viscosity of the fluid, and ∇p is the pressure gradient. The viscosity was assumed to be constant and the fluid was incompressible. The full-form of the Navier-Stokes equation is shown in Equation 9; however, this equation can be simplified under the assumption that Stokes flow (low Reynolds-number flow) is present. This condition exists in fluid flow if the Reynolds number is much less than 1. A calculation showing this to be true can be seen below, where ρ is the density of water, V is the maximum velocity of fluid in the optical trap, D is the characteristic length of the bead (calculated using the circumfrence), and μ is the dynamic viscosity of water,

$$Re = \frac{\rho VD}{\mu} = \frac{(1000)(628.31\ x\ 10^{-6})(\pi \cdot 2\ x\ 10^{-6})}{(0.001)} = 0.00395 < 1$$

Given the above calculation, the Reynolds number is much less than 1, and the Stokes flow assumption is justified. The inertial term in Equation 11 can therefore be neglected, and Equation 11 turns into,

$$\mathbf{0 = -\nabla p + F + \mu \nabla^2 v} \qquad \textbf{Equation 12}$$

The fluids were defined in the software by creating two rectangular geometries that were touching on one edge. A visual of this is shown in Figure 8. As mentioned previously, the height of fluid 1, h_1, was selected to be 900 nm, and the height of fluid 2, h_2, was selected to be 140 nm. The width of both of these sections was chosen to be the effective length of a bead in the optical trap, defined by the circumference of the bead (6.28 µm). The densities for both fluids were defined at 1000 kg/m^3 and the viscosities of fluids 1 and 2 were 0.0025 Pa·s and 0.001 Pa·s, respectively.

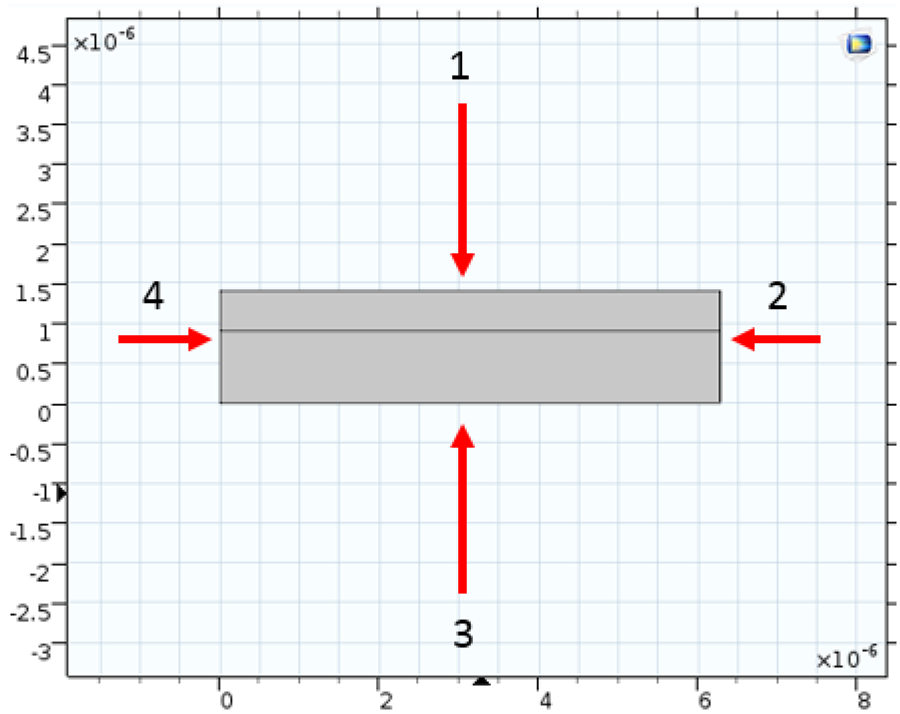

Figure 8. Diagram of the 2D Two-Fluid Couette Flow simulated in COMSOL. Each arrow shows where a boundary condition for the model was placed. Boundary 1 defines the velocity of the moving wall, boundaries 2 and 4 define the pressure gradient, and boundary 3 defines the no-slip condition.

Stokes flow and incompressible flow were assumed in the modeling of this system. A no-slip condition was placed at boundary number 3. A zero pressure boundary was applied at boundaries 2 and 4. A moving wall boundary equal to the velocity of the fluid in the optical trap (0.62831 mm/s) was applied at boundary 1. A fine mesh was used which consisted of 4934 domain elements and 414 boundary elements. The stationary study that was performed had a computation time of 6 seconds.

Computational Model of a 3D Optical Trap

A 3D model was created to simulate the stresses imposed on vWF in an optical trap. The vWF was modeled as a porous layer coating on the surface of a polystyrene bead that is subjected to fluid flow. Porous media are characterized by their specific surface and porosity[28].

For the sake of simplicity and due to the limitations of the model, these properties are assumed to be uniform, homogenous, and not to change spatially or temporally. In the optical trap, the uncoiling of vWF could change the specific surface, permeability, and porosity of the layer. These non-linearities are unknown, and so this assumption is made in order to look at the most extreme cases in which these properties could change. The polystyrene bead was fixed in place and contained a specified layer thickness of porous media around the bead. A fluid (water) given an initial inlet velocity flowed past the bead. The governing equations for the model were the Continuity equation, the Navier-Stokes equation, and the Brinkman equation, shown by Equations 13, 14, and 15, respectively,

$$\nabla \cdot \mathbf{v} = 0 \qquad \textbf{Equation 13}$$

$$\rho \frac{Dv}{Dt} = -\nabla p + F + \mu \nabla^2 v \qquad \textbf{Equation 14}$$

$$\mu \nabla^2 v - \frac{1}{K} v - \nabla p = 0 \qquad \textbf{Equation 15}$$

where K is the permeability of the media, μ is the viscosity of the fluid, and ∇p is the pressure gradient. The system is discretized in order to calculate stress values. The viscosity is assumed to be constant and the fluid is incompressible. The Continuity and Navier-Stokes equations, Equations 13 and 14, respectively, were chosen to describe the fluid flow around the media. The full-form of the Navier-Stokes equation is shown in Equation 14; however, as was done with the 2D two-fluid Couette flow model, this equation can be simplified under the assumption that Stokes flow (low Reynolds-number flow) is present. A calculation showing this to be true can be seen below, where ρ is the density of water, V is the maximum velocity of fluid in the optical trap, D is the diameter of the bead, and μ is the dynamic viscosity of water,

$$Re = \frac{\rho VD}{\mu} = \frac{(1000)(628.31\ x\ 10^{-6})(2\ x\ 10^{-6})}{(0.001)} = 0.00126 < 1$$

Given the above calculation, the Reynolds number is much less than 1, and the Stokes flow assumption is justified. The inertial term in porous media flow can therefore be neglected, and Equation 14 turns into Equation 12.

The Brinkman equation was chosen to describe the flow through the porous media. Primitive models used Darcy's law to model the porous media; however, the porous media in this application consists of void channels due to the spacing between individual vWF molecules. Fluid flow in these channels, therefore, would be incorrectly modeled by Darcy's law, because the fluid velocity using Darcy's law does not satisfy the no-slip boundary condition on the channel wall[28]. The first term in the Brinkman equation (Equation 10) accounts for these viscous forces within the media.

Initially, a stationary 2D model was created to simulate the fluid flow around the bead. Once a better understanding of the problem was obtained from the 2D model, a stationary 3D model was used to simulate this condition. The physics selected for this problem was a Fluid Flow → Porous Media and Subsurface Flow → Free and Porous Media Flow. The underlying equations for this model come from Equations 8-10.

The geometry of the model was comprised of a sphere that was 2 microns in diameter. The size of the sphere was identical to that of the experimental polystyrene bead, and was fixed in space. This constraint was performed because experimentally the bead is fixed in place due to the optical trap. A layer that was 0.1 microns thick was then added to that sphere by creating a shell. This 0.1 micron layer is representative of the porous media around the bead, and was chosen as a result of the size of vWF. vWF has been observed to be upwards of 1300 nm in length, while the globular state has been observed to be as small as 100 nm[26]. A cube that was 30 microns in length represented the domain in which the fluid was flowing. The size of this domain was selected to be large enough to include all effects from the fluid around the bead. The bead was centered inside of the cube, and the sphere was subtracted from the block using the difference tool so that the software understood that the cube and sphere were being modeled by different equations. Figure 9 shows the geometry for this model.

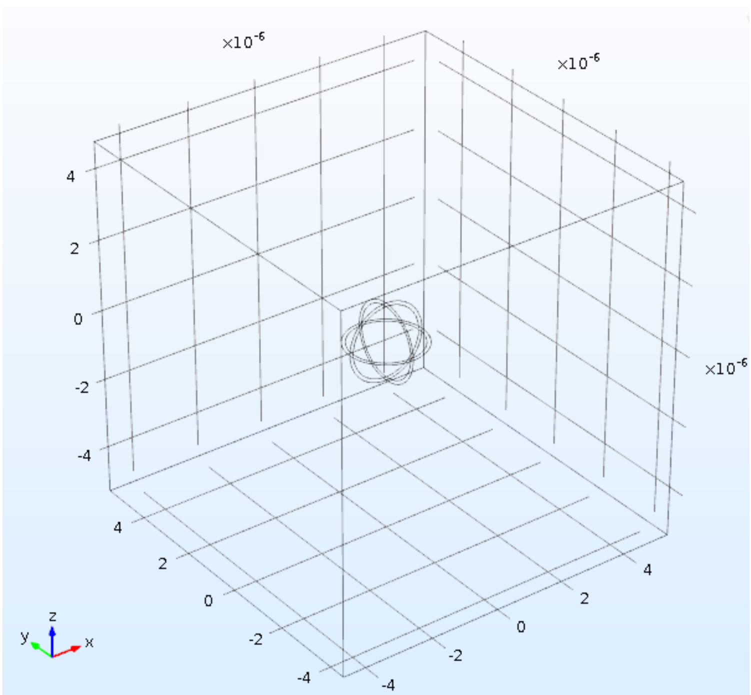

Figure 9. Geometry of a bead centrally located inside the cubic domain.

Since the polystyrene bead is fixed in the optical trap, hypothetically the bead would not move while the fluid is flowing around it. For this reason, the bead was not modeled in this simulation, and a no-slip condition was applied on that surface. This was performed as opposed to modeling the bead as polystyrene and applying deformation constraints to the surface because the inside of the bead is of no interest in this experiment, and modeling it would require additional time for the computations. As a result of this, there were only two domains: the porous layer around the bead and the fluid surrounding that layer.

Two materials were specified for this simulation. The domain of the fluid surrounding the porous layer is water. Water has a density of 1000 kg/m^3 and a dynamic viscosity of 0.001 Pa·s. The domain of the porous media was defined using a new material. In this physics, the inputs for the material, at a minimum, were porosity, dynamic viscosity, density, permeability and porosity. These input values represented the properties of the vWF shell around the bead. The porosity of this region was approximated using the size of a vWF molecule. Porosity is a measure of the open space within the medium, and is defined as the ratio of open space to total space[28]. In its globular form, vWF has been observed to have a maximal diameter ranging from 60-200 nm, while in its uncoiled state the molecules contained several subunits that were 100 nm long with globular nodules approximately 5 nm in diameter[26]. Therefore, the porosity of a vWF molecule is defined by:

$$\varepsilon = 1 - \frac{Volume\ of\ Uncoiled\ Molecule}{Volume\ of\ Coiled\ Molecule} \quad \textbf{Equation 16}$$

The volume of the coiled molecule was calculated given the maximal diameter in the coiled state (chosen as 80 nm) and assuming a spherical structure. The volume of the uncoiled molecule was calculated assuming the vWF molecule was comprised of 13 subunits (corresponding to the largest length vWF molecule) that were cylindrical in shape. The porosity was calculated to be 0.905, indicating that a globular vWF molecule is very porous.

The density of this layer was determined to be 1220 kg/m^3, as this density is most closely associated with that of proteins[29]. No evidence currently exists for the permeability value of vWF. As such, the permeability of the model was varied in the simulations. The initial permeability value for this model was assumed to be similar to that of a blood clot. The permeability of a blood clot was found to be 9.1×10^{-16} m^2, and this value defined the permeability of the vWF shell in the model[**]. The effective viscosity of the Brinkman layer was also varied in the simulations. The initial viscosity was obtained using a DNA solution in the same way that it was for the 2D two-fluid Couette flow model. The viscosity was assumed to be 0.0025 Pa·sec[27].

The inlet and outlet for the model are shown in Figure 10. The inlet condition for this model was specified to be a constant velocity of 628.31 µm/s. This inlet correlates to the velocity that Candela used in his thesis[22] to shear the beads. The outlet condition for this model was specified to be zero pressure, as no pressure gradient was assumed in the model. Open boundary conditions were assumed on the other four faces of the cube. A fine mesh was initially used for this model. The mesh, shown in Figure 11, consisted of 37113 domain elements, 1864 boundary elements, and 204 edge elements.

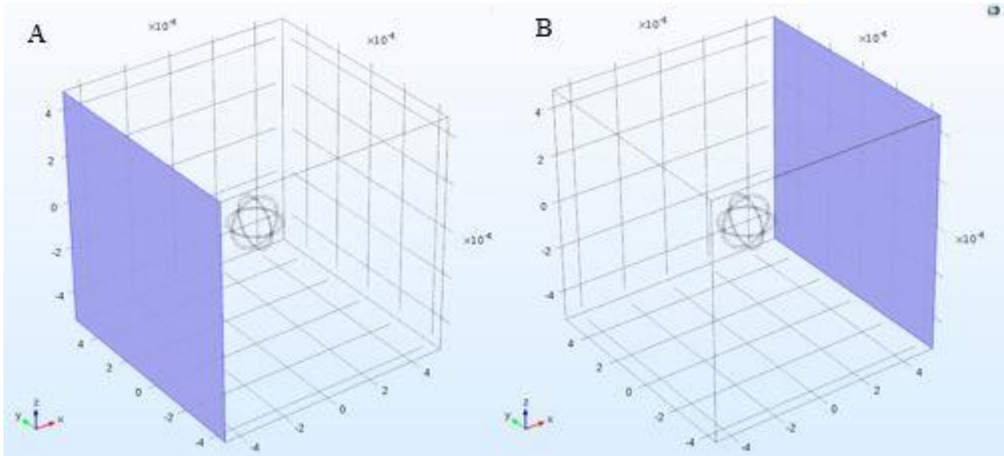

Figure 10. The locations of the (A) inlet and (B) outlet

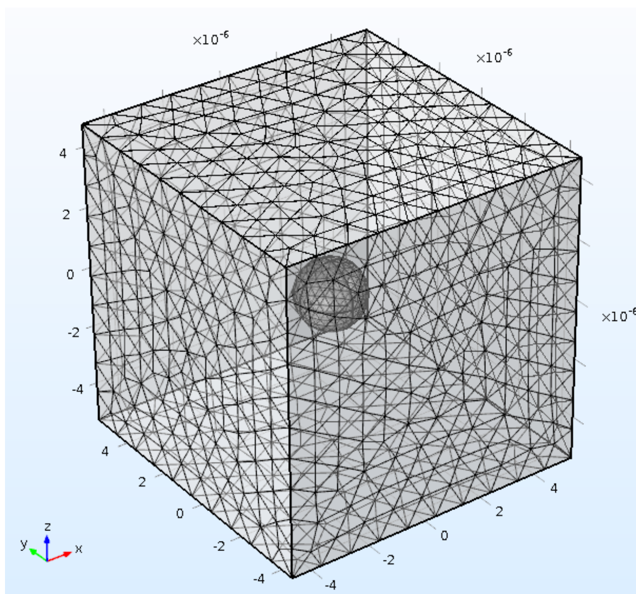

Figure 11. Fine Mesh

Chapter 3

Results

2D Two-Fluid Couette Flow

The numerical model was validated against the analytical solution to gain confidence in the computations. All of the plots for the analytical model were created in MATLAB using the code in Appendix A, which contain Equations 6 and 7. Figure 12 shows the individual velocity profiles for the numerical and analytical solutions. Figure 13 shows these two velocity plots superimposed on the same graph.

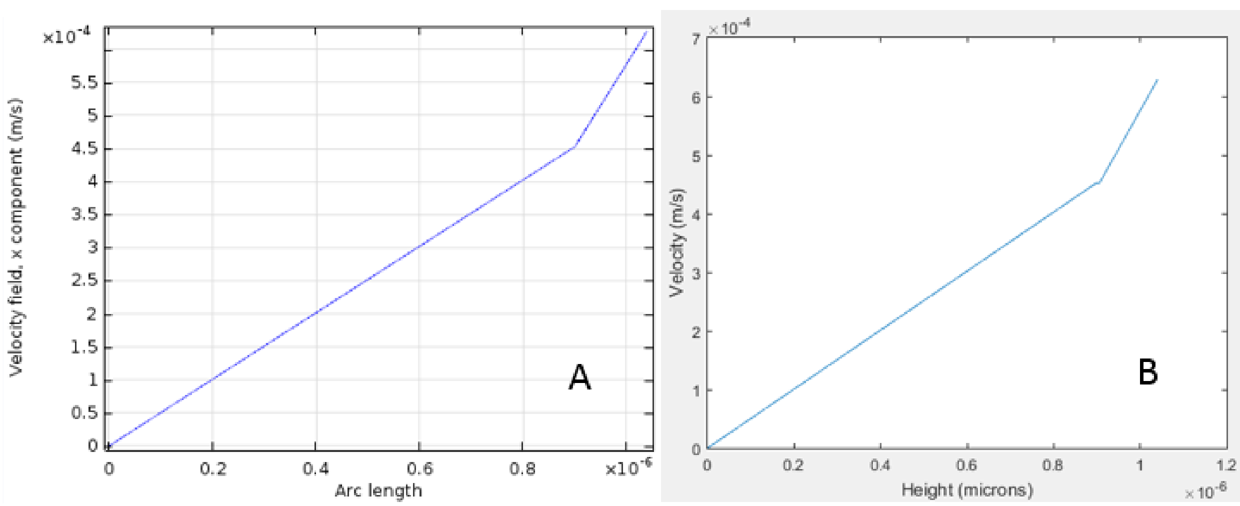

Figure 12. The velocity plots for the 2D Couette flow model produced A) numerically and B) analytically

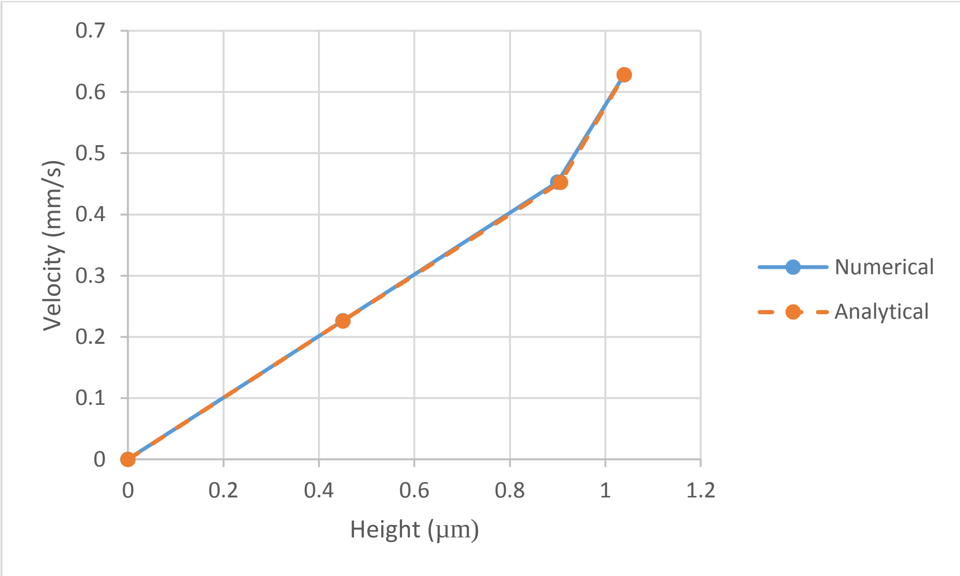

Figure 13. The analytical and numerical velocity profiles for the Couette flow situation superimposed on the same graph.

Figure 13 clearly shows the two velocity profiles agree. In addition to this qualitative plot, two locations were chosen within the Couette flow model for both models in order to further demonstrate this agreement, with one location coming from each fluid. The locations, their velocities, and the corresponding percent errors are shown in Table 1. The percent errors reflect the idea that the two velocity profiles are equal.

Table 1. The velocities at specified points for the two-fluid Couette model. The velocity values are nearly identical, and that is reflected in the percent error values.

	Analytical Velocity (mm/s)	**Numercial Velocity (mm/s)**	**Percent Error**
Location 1 (0.5·h_1)	0.22620	0.22682	0.274%
Location 1 (0.5·h_2)	0.54030	0.54255	0.416%

The shear rate was modeled for each fluid. The heights of the two fluids were specifically selected to achieve a shear rate of 1250 s^{-1} in fluid 2 through iteration of the analytical equations. Figure 14 shows the numerical shear rate values in each fluid, and that the shear rate in fluid 2 is around 1250 s^{-1}.

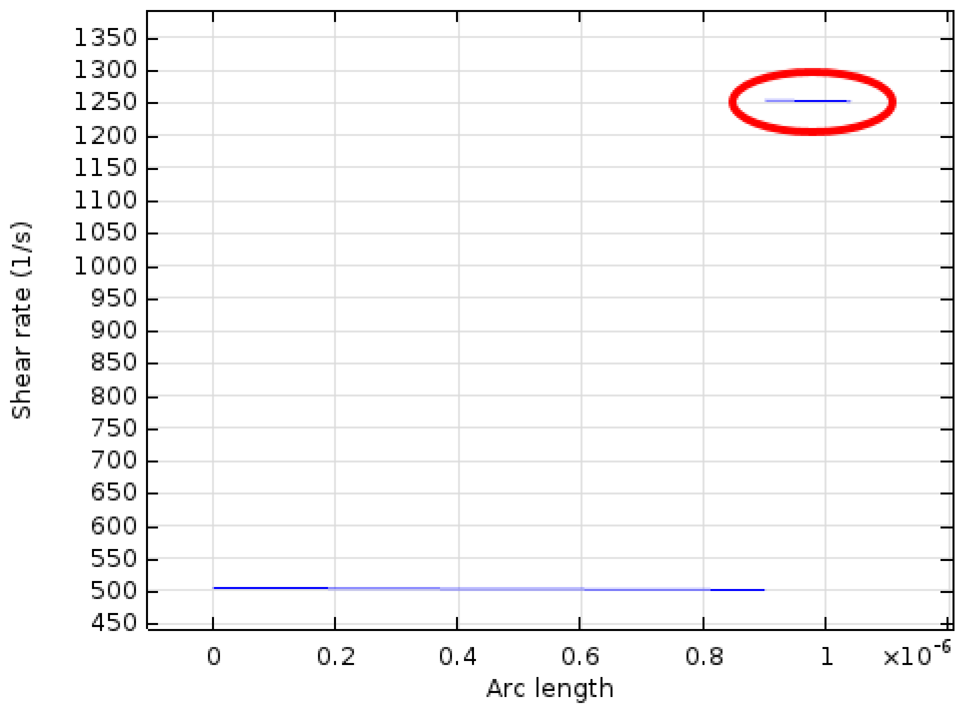

Figure 14. Plot showing the shear rates in the 2D Couette flow model. The horizontal blue line at 500 s^{-1} is the shear rate in fluid 1. The horizontal blue line at 1250 s^{-1} is the shear rate in fluid 2. The horizontal line shows that the shear rate is constant throughout the respective fluid.

This shear rate should be constant throughout each fluid given that the viscosity is constant, which is shown in Figure 14 by the horizontal line around 1250 s^{-1}. Given a constant shear rate in a particular region and constant viscosity, the shear stress can be calculated using Equation 8.

$$\tau = \mu\, \gamma = (0.001\ Pa*s)*(1250\ s^{-1}) = 1.250\ Pa = 1250\ mPa$$

This shear stress value should be constant throughout the entire fluid. This was tested by selecting five different locations within fluids 1 and 2 in the numerical model to evaluate the viscous and total stress. These are the two stress parameters that are calculated in the model. These values were compared to the analytical shear stress at the same locations. The results are summarized in Table 2.

Table 2. Comparing analytical and numerical shear stress values for selected location within the 2D two-fluid Couette flow model. The first location is within fluid 1. The next four locations are within fluid 2. The shear stress values in both of the fluids are identical.

Location in y-coordinate (μm)	**Analytical Shear Stress (mPa)**	**Numerical Viscous Stress (mPa)**	**Numerical Total Stress (mPa)**
0.45	1250	1258.0	1258.0
0.91	1250	1253.6	1253.6
0.96	1250	1253.1	1253.1
1.00	1250	1252.8	1252.8
1.03	1250	1252.5	1252.5

3D Optical Trap Model

The initial 3D optical trap model examined a 100 nm porous layer thickness. A permeability constant of 9.1 x 10^{16} m^2, porosity of 0.905, density of 1220 kg/m^3, and a viscosity of 0.0025 Pa·s were represental of the porous media. The velocity of the fluid passing the bead was 628.31 μm/s, and the flow was going from left to right. Figure 15 shows the velocity distribution within the flow chamber around a 2D model of the bead. The velocity is greatest before the bead. A boundary layer forms on the bead, and a wake forms behind the bead where the velocity is significantly decreased. A 2D cut line, as shown in Figure 16, was placed inside of the porous layer in order to characterize the velocity distribution within the porous layer. The velocity distribution can be seen in Figure 17.

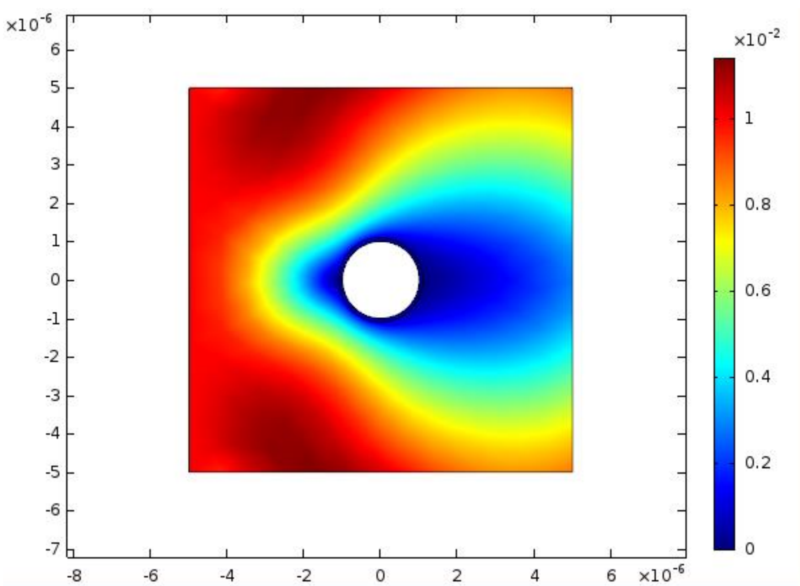

Figure 15. The velocity distribution in the flow chamber around the bead

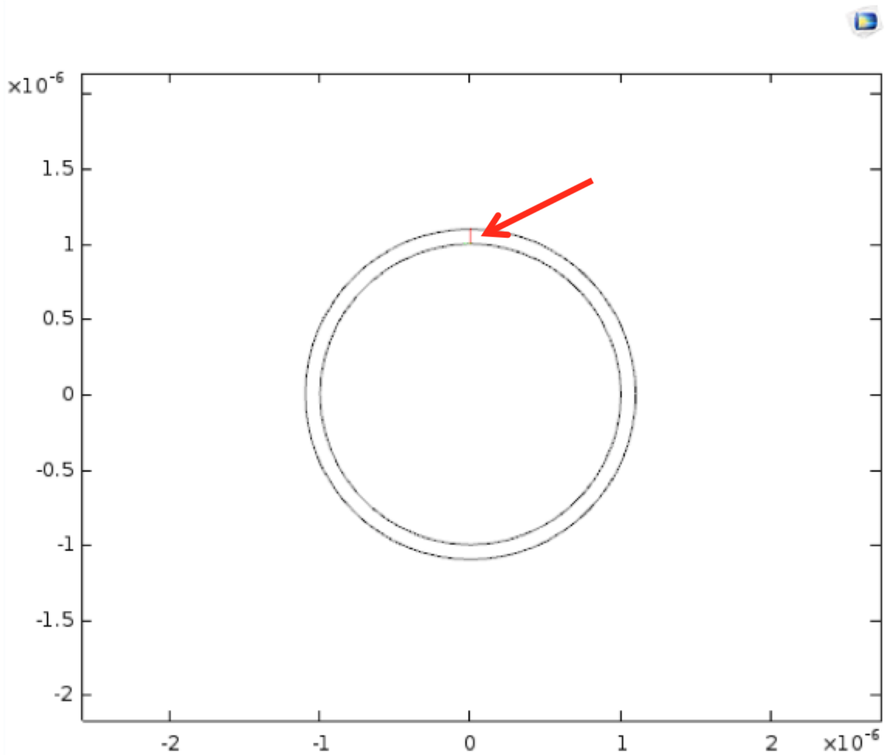

Figure 16. A red line denoting the 2D cut line used to characterize the velocity inside of the porous layer

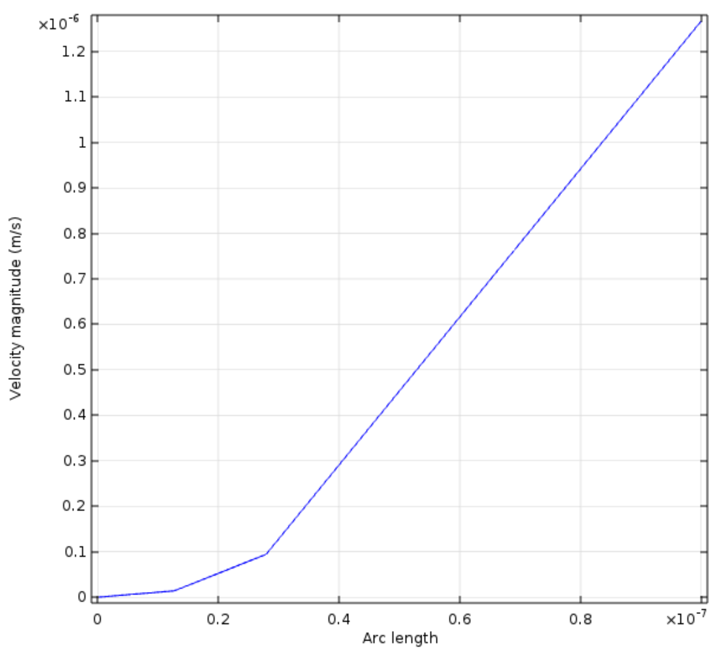

Figure 17. The velocity distribution within the porous layer

In order to determine the effect that increasing porous layer thickness has on the flow, a parametric sweep function was performed numerically to look at varying thicknesses. Eight thickness values were performed and included 100, 400, 700, 1000, 1300, 1600, 1900, and 2200 nm. The inlet velocity and conditions for the porous layer remained the same. A contour of the velocity distribution for the 100 and 2200 nm porous layers is shown in Figure 18. The stress experienced on the bead was analyzed by looking at the total force in the +x direction (going with the flow), as shown in Table 3. These force values were evaluated by performing a surface integral on the outside of the bead. Interestingly, the numerical output for force is labeled as “total stress” but uses units of Newtons. The force exerted on the bead is of interest because the algorithm that the optical trap uses calculates the drag force based on the x-direction displacement of the bead in the trap[21]. Therefore, the numerical solution models the force exerted on only the bead in the same direction as the flow. In this way, numerical and experimental values can be related.

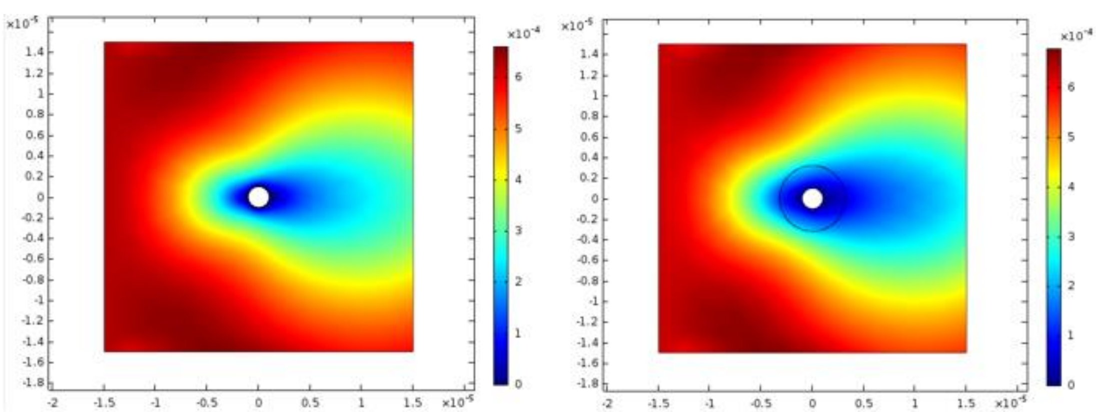

Figure 18. A visual comparison of the velocity fields surrounding a bead with A) a 100 nm porous layer and B) a 2200 nm porous layer

Table 3. Total force in the +x direction for varying layers of porous layer thicknesses

Porous Layer Thickness (nm)	Total Force (pN)
100	3.50
400	2.55
700	1.85
1000	1.40
1300	1.10
1600	0.882
1900	0.716
2200	0.602

The values for the total force shown in Table 3 were all generated numerically with the COMSOL software. The force values in the software originally contained negative signs, indicating that the stress on the bead would be in the –x direction. This negative sign was hypothesized to be a result of the sign convention that the software uses, showing that the forces calculated by the software are acting as reactive forces. In order to prove this notion, the 2D model was used to simulate stresses. The porous layer around the bead was made to be infinitesimally small in relation to the diameter of the bead. The same initial and boundary conditions were applied to the bead, as was done previously. The viscosity of the porous layer was changed to be the same as that of the outside fluid in order to avoid confounding the change in sign with the change in viscosity. During the post-processing, two surface integrals of force were calculated: the surface integral around the bead, and the surface integral around the outside of the porous layer. A diagram showing how each surface integral was taken is shown in Figure

19. Upon analysis, the two values for both forces were nearly identical in magnitude, but only differed in sign, as shown in Table 4. The surface integral around the porous media was a positive value, and the surface integral around the bead was a negative value, proving that the modeled total force on the bead was a reactive force.

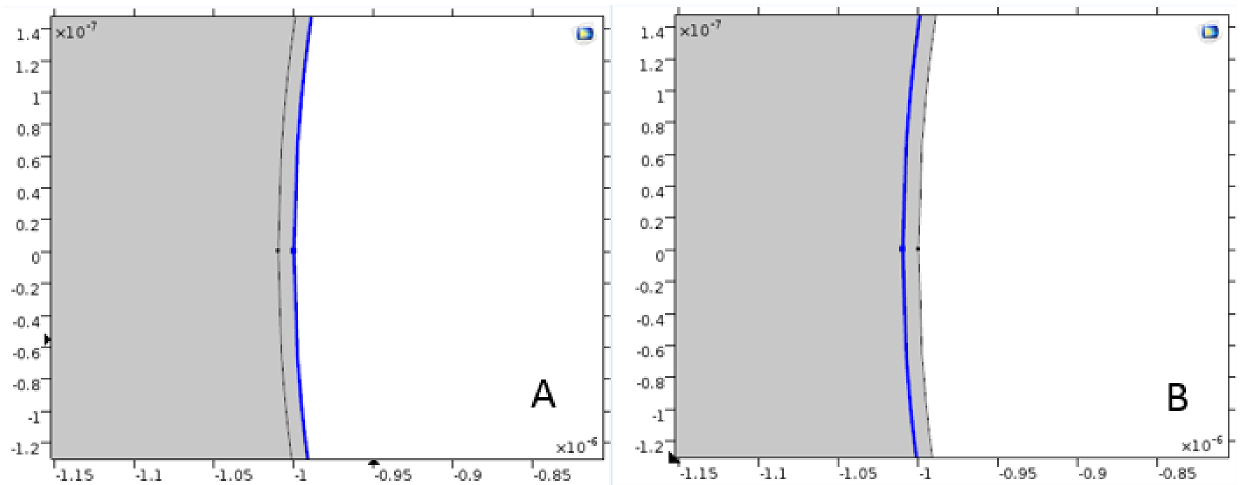

Figure 19. A 2D comparison proving that the modeled total force on the bead was a reactive force. A) shows the surface integral around the bead. B) shows the surface integral around the porous layer. These values are nearly identical in magnitude, shown in Table 4.

Table 4. Total force for the surface integral around the bead and around the porous layer for a very small porous layer. The magnitudes are nearly identical, proving that the negative force on the bead is a sign convention in the software.

	Around Bead	**Around Porous Layer**
Total Force, x component (μN/m)	-6.7922	6.7973

As discussed earlier, the values of permeability and viscosity are unknown for vWF molecules, and dependent on how many molecules of vWF is attached to the bead. The number of vWF molecules attached to the polystyrene bead experimentally is currently unknown. For this reason, different magnitudes of permeability and viscosity were inputted into the model to study their effects.

Upon further analysis of these simulations, it was observed that the velocity field inside of the porous layer was insignificant compared to the freestream velocity. Figure 17 shows the velocity profile within the porous layer at a permeability constant of 9.1 x 10^{-16} m^2. The maximum velocity value in the porous layer, which occured at the interface of the porous layer and the fluid, was approximately 0.0012 mm/s. The input velocity into the system was 0.62831 mm/s. The difference between these values is approximately three magnitudes, showing that the fluid was barely flowing through the porous media due to the low permeability.

A larger permeability was tested to study the effects. The permeability of a blood clot is very low, as the function of a blood clot is to arrest bleeding. A permeability of 1 x 10^{-7} m^2 was used for a sensitivity test. The viscosity of the porous layer was originally 0.0025 Pa·s which is greater than the viscosity of water by a factor of 2.5. In order to test the sensitivity of the porous layer to viscosity, a viscosity of 0.25 Pa·s was used.

Four conditions outlined in Table 5 were chosen to show the sensitivity of the effects of permeability and viscosity. The density and porosity values for each condition remained the same. Condition 1 consisted of the initial parameters used to obtain the values in Table 3. This condition contains the lowest permeability and viscosity values tested. In condition 2, only the value for permeability was changed from condition 1. In condition 3, only the value for dynamic viscosity was changed from condition 1. In condition 4, both the values for permeability and dynamic viscosity were changed from condition 1. The highlighted boxes in each column of Table 5 show the value that was changed with respect to condition 1. The resulting force values are shown in Table 6.

Table 5. Porous layer parameters to study the effects of permeability and viscosity on the model. The highlighted boxes in each column show the values that were changed with respect to condition 1.

	Condition 1	Condition 2	Condition 3	Condition 4
Density (kg/m^3)	1220	1220	1220	1220
Dynamic Viscosity (mPa·s)	2.50	2.50	250	250
Porosity	0.905	0.905	0.905	0.905
Permeability (m^2)	9.1e-16	1.0e-7	9.1e-16	1.0e-7

Table 6. Values for total force in the x-direction for the two conditions outlined in Table 5 at a velocity of 628.31 mm/s. Interesting to note is that for condition 1 and 3, the values decrease in magnitude as the porous layer becomes larger. For condition 2 and 4, the values increase in magnitude as the porous layer becomes larger.

	Condition 1	**Condition 2**	**Condition 3**	**Condition 4**
Porous Layer Thickness (nm)	**Total force (pN)**	**Total force (pN)**	**Total force (pN)**	**Total force (pN)**
100	3.50	11.2	3.49	11.8
400	2.55	11.7	2.56	14.1
700	1.85	13.1	1.86	18.0
1000	1.40	13.8	1.40	21.6
1300	1.10	14.9	1.11	25.8
1600	0.882	15.7	0.883	30.1
1900	0.716	16.4	0.716	34.8
2200	0.602	17.0	0.603	40.2

The results from this sensitivity study show that higher values of permeability and viscosity result in higher values of total force on the bead, and that the highest values of force occur when both the permeability and viscosity are high. Interesting to note is that at low permeabilities (conditions 1 and 3), the total force on the bead decreases as the thickness of the porous layer increases and that at higher permeabilties (conditions 2 and 4), the total force on the bead increases as the thickness of the porous layer increases.

The final model of the porous layer around the optical trap included using the viscosity of synovial fluid, which was found to be around 0.06 Pa·s (60 mPa·s)[31]. The density and porosity that have been previously defined were also used for this condition. The permeability of the porous layer was defined using 1×10^{-7} m^2, the high permeability value in Table 5. A summary of the results using this condition at the same velocity are shown in Table 7.

Table 7. Total force values for a porous layer with density = 1220 kg/m^3, permeability = 1×10^{-7} m^2, porosity = 0.905, and viscosity = 60 mPa·s at a velocity of 628.31 mm/s.

Porous Layer Thickness (nm)	Total force (pN)
100	11.6
400	13.6
700	17.1
1000	19.9
1300	23.4
1600	26.5
1900	29.7
2200	32.8

A fine mesh was used for the above analysis, and was determined to be adequate for the model. A mesh sensitivity analysis was performed and the results can be seen in Table 8. The computation time for the extra fine mesh (5 minutes and 47 seconds) was orders of magnitude higher than that of the fine mesh.

Table 8. An analysis of the mesh sensitivity. The differences between force values at the fine mesh and extra fine mesh were determined to be negligible in this study.

Porous Layer Thickness (nm)	Fine Mesh Total Force (pN)	Extra Fine Mesh Total Force (pN)	Percent Error
100	3.50	3.84	9.02%
400	2.55	2.73	6.50%
700	1.85	2.02	8.23%
1000	1.40	1.52	8.10%
1300	1.10	1.19	6.70%
1600	0.882	0.948	6.90%
1900	0.716	0.773	7.37%
2200	0.602	0.646	4.36%

Chapter 4

Discussion

Modeling of the Two-Fluid Couette Flow

The purpose of the 2D two-fluid Couette flow model was to gain a better understanding of the numerical software, COMSOL, and to determine which parameters were relevant for the optical trap simulation. A Couette flow model was chosen as it is similar to flow past a bead in an optical trap, in which one surface is stationary (the bead) and a fluid is moving with some velocity due to the movement of another surface (the fluid moving due to the oscillations of the stage). A Couette flow model was also chosen since an analytical solution exists for the problem. This analytical solution was compared to the numerical solution in order to observe any discreprencies between the two and to understand the software.

Figures 12 and 13 and Table 1 show that the velocity profiles for the analytical and computational models were identical. There was less than 0.5% error between the values of velocity at various points throughout the flow. The shear stress was calculated provided the shear rate given from the model and the viscosity of the fluid. Numerically, the software provides two types of stresses for the laminar flow physics, a viscous stress and a total stress. The COMSOL Multiphysics User Guide[32] provides definitions for both of these stresses for incompressible flow, which can be seen in Equations 17 and 18 for viscous and total stress, respectively,

$$\boldsymbol{viscous\ stress} = \boldsymbol{\mu}(\boldsymbol{\nabla u} + (\boldsymbol{\nabla u})^{\boldsymbol{T}})\boldsymbol{n} \qquad \textbf{Equation 17}$$

$$\boldsymbol{total\ stress} = (-\boldsymbol{pI} + \boldsymbol{\mu}(\boldsymbol{\nabla u} + (\boldsymbol{\nabla u})^{\boldsymbol{T}}))\boldsymbol{n} \qquad \textbf{Equation 18}$$

in which μ is the dynamic viscosity, p is the pressure, and n is the normal vector. Upon analysis, it can be seen that Equation 13 is identical to Equation 17, indicating that the viscous stress defined by the software is the same as the shear stress. This was also proved in Table 2, in which the viscous stresses generated numerically by the software were identical to shear stresses calculated analytically for a given shear rate. Table 2 also shows that the total stresses generated numerically by the software were identical to the analytical shear stresses. The reason for this is due to the boundary conditions that were put in place for the Couette flow model. A zero pressure gradient was defined in the model, therefore the pressure term in the total stress calculation disappears and the equations for total stress and viscous stress are exactly the same.

As a result of these findings, it was decided that the total stress would be used for the modeling of the 3D optical trap model. As mentioned previously, the optical trap uses an algorithm to calculate the experimental drag force on the bead[21]. The total stress generated numerically includes a viscous (shear) stress tensor in addition to a normal pressure term. This expression most closely resembles the stress that is seen in the optical trap. The stresses seen numerically and experimentally can be matched. This allows the thickness of the porous layer to be compared to the experimental effective radius of the bead to determine the actual extent of the unfurling vWF molecules.

Determining Parameters for the Optical Trap Model

The experimental effective radius of the bead is determined based on the assumption that a bead with protein adhered to the surface has a greater drag force than a non-coated bead. The protein is assumed to act as a solid surface around the bead in the calculations. The 3D model of the optical trap models this layer of protein as a porous media in order to account for fluid traveling through the layer. This more accurate representation of vWF adhered to the bead should give a better estimate of the actual height of vWF on the surface of the bead, and therefore the extent of the unfurling of these vWF molecules from an induced stress.

Table 6 shows the sensitivity of the permeability and viscosity values on the total force. At a lower permeability and viscosity (condition 1), the total force decreases in magnitude as the thickness of the porous layer increases, as opposed to at a higher permeability and viscosity (condition 4) the total force increases in magnitude as the thickness of the porous layer increases. At a low permeability, the porous layer is acting closer to a solid material, and is believed to dissipate some of the force from the fluid moving around it. Since the total force on the bead is calculated by taking the surface integral, this surface integral will decrease as the thickness of the layer increases at a low permeability. The model will output values that are similar to what would be observed with the optical trap. vWF is believed to have a porous structure in which fluid travels in between the molecules. The novelty in this model is that this fluid flow is taken into effect. Therefore, the porous layer in the simulation would have a high permeability.

Determining suitable parameters for this porous layer was critical to obtaining acceptable results. Specifically, the permeability of the layer, which indicates how easily a fluid can flow through a porous media[28], and the effective viscosity in the Brinkman layer, needed to accurately represent how the fluid would flow past the vWF molecules. The values for permeability and effective viscosity, in reality, would drastically change as the vWF molecule is unfurling from its coiled state due to the shearing from the fluid around it. These nonlinear effects are unknown, and the simulation does not account for these changes.

Since these parameters are unknown experimentally, a sensitivity study was performed in order to study how the parameters affect the model. The results from this study are shown in Table 6. The permeability values were changed by ~10 orders of magnitude, and the viscosity values were changed by two orders of magnitude. The total stress increased with increasing permeability and increasing viscosity, and those stress values appeared to decrease with thickness at low permeability but not necessarily at low viscosity. Condition 4 contains a combination of high permeability and high viscosity. The magnitude in which the total force value increased as compared to that of condition 1 was greater than that of any of the other conditions. Condition 4 shows that a potentially strong correlation exists between the permeability and viscosity values in the model. Both of these parameters are important factors to model the porous media, but the interaction between them appears to be more significant.

A final model used an input viscosity of 0.06 Pa·s based upon the viscosity found in synovial fluid[31]. Higher values of viscosity lead to larger total stress values on the bead. This value was determined to be more physiologically relevant and applicable than the previously used value. The permeability of a blood clot was originally input into the model as it was a known value of a biological permeability; however, upon analysis of the velocity profile within the porous media at this permeability, it was determined that the magnitude of this permeability may have been too low. The velocity profile within the porous layer was negligible compared to that of the free stream velocity. Under the assumption that the fluid is flowing through the vWF molecules, which is what the optical trap fails to model, the permeability value was increased.

Relating Computational and Experimental Results

The comparison between computational and experimental optical trap data was performed by first gathering relevant experimental data. Candela[22] outlines a collection of experimental data for vWF molecules attached to a bead for a variety of inlet conditions. A summary of that information is shown in Table 9.

Table 9. Experimental optical trap data obtained from Xavier Candela[22]

Shear Rate (1/s)	Velocity (μm/s)	Effective Radius w/ vWF (μm)	Effective Radius w/out vWF (μm)	Length of vWF (μm)	Drag Force (pN)
314	157.08	2.429	2.472	0.264	7.28
625	314.16	2.917	2.325	0.311	15.4
1250	628.31	3.616	2.043	1.127	36.8

The length of vWF was calculated by subtracting the effective radius of a vWF coated bead by the effective radius of a non-coated bead. The ultimate goal of this research is to relate the numerical simulation of vWF in an optical trap to the experimental data. As mentioned previously, the experimental data assumes that the densely packed vWF acts as a solid shell around the bead when determining the length of vWF (related to the effective radius observed). Assuming a solid sphere around the bead will produce a larger drag force on the bead for a given length of vWF. By simulating vWF as a porous structure, a more accurate depiction of vWF is obtained since fluid can flow within the layer of vWF. For the same length of vWF, the total force found in this simulation should be lower than the drag force found experimentally. By determining which porous layer thickness corresponds to a total force value that is the same as the drag force found experimentally, the porous layer thickness can be compared to the length of vWF for a given force. A correction factor for the length of vWF can be obtained between the numerical and experimental data. This correction factor can be used in future experiments and is essential to determining exactly how much vWF has unfurled.

A parametric sweep function has been used in the previous simulations to model different thicknesses of the porous layer. The largest porous layer thickness used in the simulations was 2.2 µm, greater than the length of vWF observed in literature. This value was determined since it could model both above and below the expected value of vWF. The final porous layer parameters used to produce the values in Table 7 were simulated at the three conditions outlined in Table 9. The results from the three conditions are shown in Table 10.

Table 10. Total force values for a given porous layer height and inlet velocity, as specified by Table 7.

	V = 157.08 µm/s	**V = 314.16 µm/s**	**V = 628.31 µm/s**
Porous Layer Thickness (µm)	**Total Force (pN)**	**Total Force (pN)**	**Total Force (pN)**
0.1	2.89	5.78	11.6
0.4	3.40	6.79	13.6
0.7	4.27	8.55	17.1
1.0	4.99	9.99	19.9
1.3	5.84	11.7	23.4
1.6	6.63	13.3	26.5
1.9	7.42	14.8	29.7
2.2	8.21	16.4	32.8

The values in Table 10 include a wide set of porous layer thicknesses to compare the experimental effective radius. Analyzing Table 9 and Table 10, the value of porous layer height that corresponds to an overlap in experimental drag force and numerical total force occurs in between 1.6-1.9 µm for the first velocity condition and 1.9-2.2 µm for the second condition. The third condition did not capture the total stress value seen in Table 9. A value would have to be extrapolated from Table 10 in order to compare to Table 9 at 628.31 µm/s; however, a porous layer thickness can be calculated by interpolation at 157.08 µm/s and 314.16 µm/s. Table 11 shows these interpolated values, the length of the vWF found experimentally from Table 9, and the correction factor between these two values.

Table 11. The porous layer thicknesses (found numericallly) and the length of vWF (found experimentally) and the corresponding correction factors at each velocity.

Velocity (µm/s)	Force (pN)	Thickness of Porous Layer (µm)	Length of vWF (µm)	Correction Factor
157.08	7.28	1.85	0.264	7.00
314.16	15.4	2.00	0.317	6.32
628.31	36.8	>2.20	1.127	>1.95

Based on the data in Table 11, a factor to correct the experimental values for vWF unfurling was obtained. These values, which are intended to be more representative of the optical trap situation and the unfurling of vWF, show that the experimental data is underestimating the degree of vWF unfurling. This agrees with the hypothesis mentioned above; that assuming vWF is a solid sphere would result in larger stresses for a given length of vWF, and consequently would result in lower lengths of unfurled vWF for a given force as opposed to modeling the protein as a porous media.

However, even though a correction factor was obtained, the porous layer thickness observed was much larger than the length of vWF that has been observed in literature (1.3 µm). Since the amount of vWF on the bead and the mechanism in which the molecule is adhered to the surface is unknown, the exact reason for this remains unknown. Depending on how much vWF is adhered to the surface of the bead, the individual molecules may be anchored to the bead in more than one location. Due to the shear number of vWF that may exist on the bead, these molecules could also be in an overlapping orientation. In both of these cases, the mechanism of vWF unfurling may be different than what has been observed in literature. The vWF optical trap literature that currently exists describes methods for opening up the A2 domain and shearing a single molecule of vWF[20]. The optical trap in this instance is used to shear multiple molecules of vWF that are in an unknown configuration. Therefore, the 21 pN unloading force[14] and 1300 nm length of a single vWF molecule[26] observed in literature may be invalid. Another consideration is that the model is looking at extreme conditions since the non-linearities of how these properties change in time is unknown. More information about the structure of vWF on the bead and how the properties change in time is necessary in order to create a more representative model.

Although the porous layer thickness values are out of range, the correction factors found for 314 s^{-1} and 625 s^{-1} are consistent. Assuming that the correction factor is constant regardless of the shear rate, a total force value would not be obtained for the given porous layer thicknesses at 1250 s^{-1}. The experimental length of vWF from Table 11 was observed to be 1.1271 µm. Using the correction factor from 314 s^{-1} and 625 s^{-1}, the porous layer thickness would be required to be around 6-7 µm, which was not observed in this experiment.

Mesh Sensitivity

The mesh sensitivity in Table 8 shows a percent difference in the total force value between the fine and extra fine mesh to be between 4-10%. The fine mesh was determined to be adequate for these simulations. The reason for this is because preliminary simulations were looking at the relative magnitudes of total stress and the sensitivity of the parameters. When comparing the numerical data to the experimental data, the difference between the data was so large that a finer mesh would not have provided much additional insight into relating the magnitudes of the forces. The mesh served to characterize the sensitivity of the parameters and the relative magnitudes. When more accurate parameters are determined in the future, a finer mesh should be considered in order to obtain a more accurate correction factor.

Chapter 5

Conclusion

Computational results from this research provide an initial model for predicting the actual extent to which vWF is unfurling inside of the optical trap by modeling flow through the vWF molecules. The model should be able to take experimental drag force data from the optical trap and find the thickness of the porous layer in the model that correlates to the effective radius observed experimentally. A correction factor can be determined and used to calculate the actual unfurling length of vWF. The model was validated using a simpler two-fluid Couette flow model in which the analytical solution was compared to the numerical solution. This was done in order to better understand the COMSOL software used for numerical modeling.

This study shows that the experimental optical trap model is underestimating the unfurling of the vWF molecules. This indicates that at a given drag force, vWF molecules are unfurling to a greater extent than calculated by the optical trap. The numerical model is sensitive to changes in permeability and viscosity of the porous layer modeling vWF, and the interaction between those variables appears to be significant. Representative values for the parameters of this porous layer were obtained in order to accurately model the vWF around the bead. This model and the correction factor can be used to determine the actual unfurling of vWF on an optical trap for a given experimental dataset. Understanding how vWF is unfurled and sheared experimentally provides insight into some of the clinical problems associated with medical devices, such as VADs, such that the devices can be designed for safety and efficacy.

Chapter 6

Future Work

Future work should look into determining the actual parameters of a vWF layer on a bead. All of the porous layer parameters, including permeability, porosity, density and viscosity, drastically change depending on the orientation of vWF in the trap and the rate of unfurling. As mentioned above, these values are unknown and have not been extensively studied. A better understanding of what these values are could be obtained by quantifying the amount of vWF on a bead. With this information, an experiment could be setup in which a solution of vWF molecules are anchored to a surface and a viscometer could measure the viscosity of this solution. Using this same concept, a test for permeability of this layer could also be performed. A control for the experiment, such as a bead covered in DNA (streptavidin), could also provide a reference and control for how much vWF is unfurling.

In addition to gaining a better understanding of the parameters of the porous layer, more experimental optical trap data should be obtained in order to compare the two datasets. The sample size of experimental data obtained was limited which may have significantly impacted the validity of the model. In addition, the experimental data shown in Table 9 showed that the effective radius of the bead without vWF was over 2 µm, when it is known that the radius of the bead is 1 µm. This discreprency could possibly have invalidated the experimental data used in this study. By using more experimental data, a greater confidence in the length of vWF observed experimentally and the corresponding correction factors can be obtained.

A sensitivity study was outlined in this work to examine the effect that two of the porous layer parameters exhibited on the model. The results from the study showed that the parameters each independently affected the model, but that the interaction between the two parameters appeared to be most significant. With this information, future work should statistically look into the significance of these parameters and their interactions to study any linear or quadratic effects. This information would provide insight into which porous layer parameters are the most significant in the model.

COMSOL Multiphysics provides a Free and Porous Media Flow physics that can accurately model a porous layer; however, manipulating equations in the software was not always user friendly. Once a physics was chosen, the governing equations and post-processing outputs were already defined for the simulation. Overriding an equation or a parameter was difficult to perform. Another FEA package that allows the user to have more control over the equations and how the software is using these equations may provide a simpler model.

In addition to comparing computational to experimental values, a number of papers in literature were found that derived solutions for flow past a porous sphere using the Brinkman equation[33,34]. These papers explicitely look at flow past a completely porous sphere. In the case of the optical trap and the model that was created, these papers were not directly related since there is a bead inside of the porous sphere; however, they may provide insight into the stresses that are observed. They could also provide another option for validating a solution.

The physics chosen for this model was a Free and Porous Media Flow that consisted of the Continuity, Navier-Stokes, and Brinkman equations. Other equations, such as Darcy's law, were not used to model the situation due to the assumptions that were made. In addition, a number of other physics offered through COMSOL, such as Darcy's Law, Biot Poroelasticity and Viscoelastic Fluid, were originally considered. Given a set of different assumptions, one of these physics may more accurately represent the situation.

Experimental information on the drag force associated with polystyrene beads without vWF exists in Candela's thesis[22]. As a result of this, a 3D model of the bead without a porous layer of vWF could be modeled numerically in COMSOL. This simulation should theoretically produce total force values that are identical to the drag force values obtained experimentally. This information could be used to validate the optical trap model outlined in this work. Any discreprencies between the numerical and experimental data for that model could provide insight into some of the discreprencies observed in the model presented in this thesis.

Appendix A

MATLAB Code for Plotting 2D Couette Flow Velocity Profile

```
%Determining velocity profiles for 2D two-fluid Couette flow

V = 0.62831e-3; %inlet velocity

mu1 = 0.0025; %viscosity of fluid 1
mu2 = 0.001; %viscosity of fluid 2
h1 = 0.9e-6; %height of fluid 1
h2 = 0.14e-6; %height of fluid 2

y1 = linspace(0,h1,135); %scaling the y-coordinate values in fluid 1 based on
the heights
y2 = linspace(h1,h1+h2,21); %scaling the y-coordinate values in fluid 2 based
on the heights
y = linspace(0,h1+h2,156); %combined y-matrix

u1 = ((mu2*V)/(mu2*h1+mu1*h2))*y1; %analytical velocity of fluid 1
u2 = (V/(mu2*h1+mu1*h2))*(mu1*(y2-h1)+mu2*h1); %analytical velocity of fluid2
u11 = horzcat(u1,u2); %combined velocity matrix
plot(y,u11)
xlabel('Height (microns)')
ylabel('Velocity (m/s)')
```

BIBLIOGRAPHY

1. National Heart, Lung, and Blood Institute. Disease Statistics. 2012 NHLBI Fact Book, Chapter 4, Disease Statistics, NHLBI, NIH; 2012.
2. US Department of Health and Human Services. A Public Action Plan to Prevent Heart Disease and Stroke. Atlanta, GA: US Department of Health and Human Services, Centers for Disease Control and Prevention; 2003.
3. National Heart, Lung, and Blood Institute. How to Prevent and Control Coronary Heart Disease Risk Factors. NHLBI, NIH; 2015. From http://www.nhlbi.nih.gov/.
4. National Health Service. Heart Transplant – Risks. 2014. From http://www.nhs.uk/.
5. V Kilic, Ahmet; Emani, Sitaramesh; Sai-Sudhakar, Chittoor B; Higgins, Robert S D; Whitson, Bryan A (2014) *Journal of thoracic disease* vol. 6 (8) p. 1097-104
6. United Network of Organ Sharing. Transplant Trends. 2015. From https://www.unos.org/.
7. F Loor, G., & Gonzalez-Stawinski, G. (2012). Pulsatile vs. continuous flow in ventricular assist device therapy. *Best Practice & Research. Clinical Anaesthesiology*, *26*(2), 105–15.
8. Slaughter MS, Rogers JG, Milano CA. Advanced Heart Failure Treated with Continuous-Flow Left Ventricular Assist Device. New England Journal of Medicine. 2009; 361(23): 2241-2251.
9. Uriel, N., Pak, S.-W., Jorde, U. P., Jude, B., Susen, S., Vincentelli, A., … Mancini, D. (2010). Acquired von Willebrand syndrome after continuous-flow mechanical device support contributes to a high prevalence of bleeding during long-term support and at the time of transplantation. *Journal of the American College of Cardiology*, *56*(15), 1207–13.

10. Geisen, U., Heilmann, C., Beyersdorf, F., Benk, C., Berchtold-Herz, M., Schlensak, C., Zieger, B. (2008). Non-surgical bleeding in patients with ventricular assist devices could be explained by acquired von Willebrand disease. *European Journal of Cardio-Thoracic Surgery: Official Journal of the European Association for Cardio-Thoracic Surgery*, *33*(4), 679–684.
11. Tsai, H. M. (1996). Physiologic cleavage of von Willebrand factor by a plasma protease is dependent on its conformation and requires calcium ion. *Blood*, *87*(10), 4235–4244.
12. Sadler, J. E. (1998). Biochemistry and Genetics. Biochemistry, 395–424.
13. De Meyer, S. F., Stoll, G., Wagner, D. D., & Kleinschnitz, C. (2012). von Willebrand Factor: An Emerging Target in Stroke Therapy. *Stroke*, *43*(2), 599–606.
14. Ying, J., Ling, Y., Westfield, L. a, Sadler, J. E. & Shao, J.-Y. Unfolding the A2 domain of von Willebrand factor with the optical trap. *Biophys. J.* **98,** 1685–93 (2010).
15. Zanardelli, S., Chion, A. C. K., Groot, E., Lenting, P. J., Mckinnon, T. a. J., Laffan, M. a., … Lane, D. a. (2009). A novel binding site for ADAMTS13 constitutively exposed on the surface of globular VWF. *Thrombosis and Haemostasis*, *114*(13), 2819–2828.
16. Tsai, H. M., Sussman, I. I., & Nagel, R. L. (1994). Shear stress enhances the proteolysis of von Willebrand factor in normal plasma. *Blood*, *83*(8), 2171–2179.
17. Heilmann, C., Geisen, U., Beyersdorf, F., Nakamura, L., Benk, C., Berchtold-Herz, M., … Zieger, B. (2010). Acquired von Willebrand syndrome in patients with ventricular assist device or total artificial heart. *Thrombosis and Haemostasis*, *103*(5), 962–967.
18. Selgrade, B. P., & Truskey, G. a. (2012). Computational fluid dynamics analysis to determine shear stresses and rates in a centrifugal left ventricular assist device. *Artificial Organs*, *36*(4), E89–96.

19. Siedlecki CA, Lestini BJ, Kottke-Marchant KK, Eppell SJ, Wilson DL, Marchant RE. Shear-dependent changes in the three-dimensional structure of human von Willebrand factor. Blood. 1996; 88(8): 2939-2950.

20. Zhang, X., Halvorsen, K., Zhang, C.-Z., Wong, W. P. & Springer, T. a. Mechanoenzymatic cleavage of the ultralarge vascular protein von Willebrand factor. *Science* **324,** 1330–4 (2009).

21. Corsetti, Monica. An Experimental Setup to Test the Effects of Shear Stress on von Willebrand Factor. The Pennsylvania State University, University Park, 2014.

22. Candela, Xavier. The Investigation of Fluid Shear Stress and Subsequent Conformational Changes of von Willebrand Factor Observed in an Optical Trap. The Pennsylvania State University, University Park, 2016.

23. Ferko, M. C., Bhatnagar, A., Garcia, M. B., & Butler, P. J. (2007). Finite-element stress analysis of a multicomponent model of sheared and focally-adhered endothelial cells. *Annals of Biomedical Engineering*, *35*(2), 208–23.

24. Weinbaum, S., Zhang, X., Han, Y., Vink, H., & Cowin, S. C. (2003). Mechanotransduction and flow across the endothelial glycocalyx. Proceedings of the National Academy of Sciences of the United States of America, 100(13), 7988–7995.

25. Cengel, Y. A., J. M. Cimbala. "Fluid Mechanics: Fundamentals and Applications". 2nd Ed., McGraw-Hill, 2009.

26. Slayters, H., Loscalzoyl, J., Bockenstedt, P., & Handin, R. I. (1985). Native Conformation of Human von Willebrand Protein a, (14), 8559–8563.

27. Goodman, A., Tseng, Y., & Wirtz, D. (2002). Effect of Length , Topology , and Concentration on the Microviscosity and Microheterogeneity of DNA Solutions, *2836*(02), 199–215.

28. Truskey, George A., Fan Yuan and David Katz. *Transport Phenomena in Biological Systems*. New Jersey: Pearson Prentice Hall, 2004. Print.

29. Quillin, M. L., & Brian, W. (2000). Accurate calculation of the density of proteins, 791–794.

30. Webster, M. W., & Med-, C. C. (n.d.). Cellular content and permeability of intraluminal thrombus in abdominal aortic aneurysm. 1996.

31. Vincent, H. K., Percival, S. S., Conrad, B. P., Seay, A. N., Montero, C., & Vincent, K. R. (2013). Hyaluronic Acid (HA) Viscosupplementation on Inflammation in Knee Osteoarthritis : A Pilot Study Synovial Fluid, 378–384.

32. COMSOL Multiphysics User's Guide. COMSOL AB. 2012.

33. Phys, M. Stokes flow past a porous sphere using Brinkman's model. By B.S. Padmavathi, T . Amaranath and S . D . Nigam , School of Mathematics and Computer / Information Sciences , University of, *44*. 1993.

34. Yu, Q. I. N. A Cartesian-tensor solution of the Brinkman equation, *188*, 177–188. 1988.

ACADEMIC VITA

Michael W. Tramontozzi

www.linkedin.com/in/tramontozzimichael | mwt5218@psu.edu | (860) 823-9334

EDUCATION

B.S., Biomedical Engineering (May 2016)
B.S., Mechanical Engineering (May 2016)
The Pennsylvania State University, State College, PA
Schreyer Honors College

EXPERIENCE

W. L. Gore & Associates, Engineering Intern
Gore Medical Products Division, Elkton, MD **May 2015-August 2015**

- *New Product Development for a soft tissue repair device in design control:*
  - Correlated fitness for use (FFU) surgical performance to mechanical properties of raw materials.
  - Created manufacturing process limits for raw materials with Design of Experiment (DOE) development and analysis.
  - Drove decision to utilize currently unused manufacturing equipment through cross-functional team discussion.
  - Executed a validation protocol and implemented a validation report into the quality system.
  - Identified potential ways to triple process throughput through experimental design and modeling.

W. L. Gore & Associates, Engineering Intern
Gore Medical Products Division, Flagstaff, AZ **May 2014-August 2014**

- *New Product Development for a vascular stent in design control:*
  - Conducted a DOE of 160 samples to evaluate the effect of process factors on product responses.
  - Proposed a new material product specification by analyzing experimental data.
  - Justified a design output change using experimental and historical data.
  - Executed preliminary Operational Qualification (OQ) work for manufacturing equipment.
  - Built, tested, and deployed full prototype devices to assess technical feasibility.
  - Modeled a clinical outcome using *in vitro* techniques.

Johnson & Johnson, Research & Development (R&D) Co-op
McNeil Consumer Healthcare, Fort Washington, PA **June 2013-December 2013**

- *Application lead for the re-introduction of a global multi-active drug product:*
  - Implemented an analytical tool into the design process to ensure upstream product quality.
  - Saved the team $16,000 through manufacturing process improvements.
  - Interfaced cross-functionally with the marketing team to target consumer needs.

Artificial Heart and Cardiovascular Fluid Dynamics Laboratory, Research Assistant
Pennsylvania State University, University Park, PA **September 2012-present**

- *Identify safe levels of non-physiological shear induced by ventricular assist devices (VADs):*
  - Created an *in vitro* VAD model using a syringe pump and capillary tubing.
  - Modified protocols to characterize how varying levels of shear affect blood coagulation.

- Collaborated with surgeons from the Hershey Medical Center on total artificial heart development research.

LEADERSHIP & INVOLVEMENT

President – McNeil Consumer Healthcare Intern/Co-op Association (ICA) Board, **2013**
Social Media Chair – McNeil Consumer Healthcare Intern/Co-op Association (ICA) Board, **2013**
Organization Chair – Penn State IFC/Panhellenic Dance Marathon, **2011-2013**
Parade Ground Liaison – Penn State Homecoming Parade, **2014**
Solicitation Chair – Penn State IFC/Panhellenic Dance Marathon, **2015**
Member – Biomedical Engineering Society, Penn State Chapter, **2011-2015**
Member – Penn State Italian Student Society, **2011-2015**
Donor & Alumni Relations Captain – Penn State IFC/Panhellenic Dance Marathon, **2015-2016**

SKILLS

Microsoft Office
Software – MATLAB • SolidWorks • JMP Statistical Software • R Statistical Software • COMSOL • ANSYS
Testing – Instron • Rheometer • Microscopy (SEM) • Gel Electrophoresis • Western Blot